HHS Public Access

Author manuscript

Nature. Author manuscript; available in PMC 2024 November 01.

Published in final edited form as:

Nature. 2024 May ; 629(8012): 710–716. doi:10.1038/s41586-024-07374-4.

Structural basis of lipid head group entry to the Kennedy pathway by FLVCR1

Yeeun Son[1,2], **Timothy C. Kenny**[3], **Artem Khan**[3], **Kıvanç Birsoy**[3], **Richard K. Hite**[1,*]

[1]Structural Biology Program, Memorial Sloan Kettering Cancer Center, New York, NY, USA

[2]BCMB Allied Program, Weill Cornell Graduate School, New York, NY, USA

[3]Laboratory of Metabolic Regulation and Genetics, The Rockefeller University, New York, NY, USA

Summary

Phosphatidylcholine and phosphatidylethanolamine, the two most abundant phospholipids in mammalian cells, are synthesized *de novo* by the Kennedy pathway from choline and ethanolamine, respectively[1–6]. Despite the essential roles of these lipids, the mechanisms that enable the cellular uptake of choline and ethanolamine remain unknown. Here, we show that FLVCR1, whose mutation leads to the neurodegenerative syndrome PCARP[7–9], transports extracellular choline and ethanolamine into cells for phosphorylation by downstream kinases to initiate the Kennedy pathway. Structures of FLVCR1 in the presence of choline and ethanolamine reveal that both metabolites bind to a common binding site comprised of aromatic and polar residues. Despite binding to a common site, the larger quaternary amine of choline interacts differently with FLVCR1 than does the primary amine of ethanolamine. Structure-guided mutagenesis identified residues that are critical for the transport of ethanolamine, while being dispensable for choline transport, enabling functional separation of the entry points into the two branches of the Kennedy pathway. Altogether, these studies reveal how FLVCR1 is a high-affinity metabolite transporter that serves as the common origin for phospholipid biosynthesis by two branches of the Kennedy pathway.

Phospholipids are integral components of membranes, whose amphipathic nature establishes barriers between cells and their environment and between subcellular compartments within cells. The two most common phospholipids in mammalian cells are phosphatidylcholine (PC) and phosphatidylethanolamine (PE), which together account for between 55-75% of

*Correspondence: hiter@mskcc.org, Correspondence and requests for materials should be sent to R.K.H.

Author contributions

Conceptualization, Y.S. and R.H.; Methodology Y.S., T.K., A.K., K.B. and R.H., Formal Analysis, Y.S. and R.H.; Investigation, Y.S., T.K., K.B. and R.H.; Writing – Original Draft, Y.S. and R.H.; Funding Acquisition, T.K., K.B. and R.H.

Competing interests

R.K.H is a consultant for F. Hoffmann-La Roche Ltd. K.B. is scientific advisor to Nanocare Pharmaceuticals and Atavistik Bio. Other authors declare no competing interests.

Code availability

The code used for the Github link to the code for FLVCR1 DepMap Coessentiality analysis is available at https://github.com/artemkhan/Coessentiality_DepMAP_FLVCR1.git.

the total phospholipid content[1,2]. PC and PE are synthesized *de novo* by the three-step Kennedy pathway from choline and ethanolamine via phospho- and cytidine-diphospho-intermediates[3–6]. Choline can also contribute to the biosynthesis of other phospholipids and sphingolipids, one-carbon metabolism, and neurotransmitter synthesis[10]. We and others recently identified the ubiquitously expressed feline leukemia virus subgroup C cellular receptor 1 (FLVCR1) and its close paralog FLVCR2 as plasma membrane transporters that facilitate the uptake of extracellular choline into cells[11,12]. FLVCR1 is essential for viability in mice, and mice lacking functional FLVCR1 die around embryonic day E12.5[11]. In humans, several point mutations have been identified in FLVCR1 that lead to posterior column ataxia and retinitis pigmentosa (PCARP), an autosomal-recessive neurodegenerative syndrome that is initiated during childhood and results in loss of vision, abnormal proprioception, and muscle atrophy[7–9]. Mutations in FLVCR2 can lead to Fowler syndrome, a vascular disorder characterized by severe hydrocephaly, hypokinesia, and arthrogryposis[13–15].

FLVCR1 is a member of the major facilitator superfamily (MFS) of membrane transporters that are characterized by possessing two bundles of six transmembrane helices (6TM) connected by an extended intracellular linker. Humans express over 100 MFS transporters that transport diverse substrates ranging from ions to sugars to porphyrins[16]. Structures of MFS transporters from different phyla resolved in inward-facing, occluded, and outward-facing states have revealed a conserved rocker-switch alternating access transport mechanism where the two 6TM bundles rock around a central substrate binding site to alternatively allow access from either the extracellular or intracellular side of the membrane[16–18]. Substrate transport by MFS transporters can be actively coupled to the symport or antiport of a second substrate, such as a proton, or can be passively coupled to electrochemical gradients[19]. For FLVCR1, the mechanisms of substrate recognition and transport are poorly understood. Here, we combine cryo-EM structural, biochemical, and metabolomic analyses to investigate the uptake of choline by FLVCR1. These studies unexpectedly revealed that FLVCR1 is also an ethanolamine transporter that can serve as the primary ethanolamine transporter in cells.

FLVCR1 transports choline

To investigate the ability of FLVCR1 to directly transport choline, we reconstituted purified human FLVCR1 into lipid vesicles. FLVCR1-containing and protein-free liposomes were then incubated with radiolabeled choline ([methyl-^{3}H]choline) for up to 1 hour. We observed a time-dependent increase in choline uptake into the vesicles containing FLVCR1 that was absent in the protein-free vesicles (Fig. 1a). We next examined the effects of pH, cations, and membrane potential on choline transport. By varying the pH of the external solution from 4.5 to 10.5, while maintaining an internal pH of 7.5, we found choline transport by FLVCR1 is not proton-coupled (Extended Data Fig. 1). To determine if choline transport by FLVCR1 is coupled to the movement of Na^+, as occurs in the cholinergic neuron specific choline transporter, CHT1[20–22], we replaced the K^+ in the external solution with Na^+, finding that choline uptake was similar in both conditions. We also examined the effect of divalent cations, finding that uptake rates were similar when experiments were performed in the presence of either Ca^{2+} or Mg^{2+}. However, when we replaced the K^+ in the external

solution with Na^+ and added the K^+ ionophore valinomycin, we observed an increase in choline uptake, suggesting that choline uptake can be accelerated by negative membrane potentials (Fig. 1a). Together, these data indicate that FLVCR1 is a passive facilitator that takes advantage of the resting negative membrane potential and of the choline gradient between the extracellular solution, which contains 10 μM choline in plasma[23–26], and the cytosol, which has low choline concentrations due to the phosphorylation of choline by choline kinase alpha[27].

Structure of choline-bound human FLVCR1

To determine the mechanisms of choline recognition and transport, we collected cryo-EM images of detergent-solubilized human FLVCR1 in the presence of 1 mM choline chloride (Extended Data Figs. 2 and 3). Iterative classification of particles extracted from these images resulted in a single class whose reconstruction achieved a resolution of 2.60 Å that was suitable for building and refining a *de novo* model of human FLVCR1 with good geometry (Fig. 1b–d, Extended Data Figs. 2 and 3, and Extended Data Table 1). Similar to other members of the MFS superfamily, FLVCR1 is comprised of two 6TM domains that are connected by a flexible intracellular linker, with TM1-TM6 forming the N-terminal domain (NTD) and TM7-TM12 forming the C-terminal domain (CTD). The NTD and CTD are structurally homologous, with an RMSD of 3.5 Å, creating a pseudo-two-fold symmetry axis through the center of the transporter (Extended Data Fig. 4). A cavity extending from the cytosolic side of the transporter can be observed along this central axis between the two domains (Fig. 1e). This central cavity extends more than 30 Å into the transporter and is highly electronegative due to six aspartate and glutamate residues within and near the cavity (Fig. 1e and Extended Data Fig. 4). The minimum radius of the cavity is 2.1 Å, which may be wide enough to accommodate a choline molecule. The extracellular side of the cavity is sealed by TM1 and TM7, which adopt kinked conformations that bring them into direct contact near their extracellular ends (Fig. 1f).

Several non-protein densities can be observed in the cytosolic cavity, including one at the top of the central cavity that we assigned as a choline molecule based on its shape (Fig. 1f). We will therefore refer to this state as a choline-bound state. The hydroxyl group of the bound choline interacts with the side chains of Gln214 and Gln471, while the quaternary amine forms cation-π interactions with the side chains of Trp125 and Tyr349 (Fig. 1g–h). Also contributing to the binding site are Tyr153, Met154, and Asn245. The substrate-binding residues are conserved in FLVCR2, suggesting that the paralogs share a conserved substrate-binding site (Extended Data Fig. 5). This combination of aromatic and polar residues is reminiscent of the choline-binding sites in the prokaryotic periplasmic choline-binding protein ChoX from *S. meliloti* (PDB: 2REG) and the prokaryotic choline transporter LicB from *S. pneumoniae* (PDB: 7B0K), both of which are evolutionarily distinct from FLVCR1[28,29].

We next performed a DALI search to identify homologous structures deposited in the Protein Data Bank, finding that the two most homologous structures are two prokaryotic MFS transporters in inward-facing states: *E. coli* SotB (PDB: 6KKL; RMSD = 2.3 Å), a drug-proton antiporter, and *E. coli* DgoT (PDB: 6E9N; RMSD = 2.6 Å), a D-galactonate

transporter[30–32] (Extended Data Fig. 4). Taken together with the open cytosolic cavity and the occupied substrate-binding site, we assign the structure determined in the presence of 1 mM choline as an inward-facing, choline-bound state.

Endogenous ligand-bound structures

For importers, an inward-facing, substrate-bound structure corresponds to a state following substrate binding and translocation from the extracellular space but prior to release into the cytosol. To gain additional insights into the transport mechanism, we next collected cryo-EM images of FLVCR1 in the absence of exogenous substrate. Iterative classification of the particle images resulted in two distinct states (Fig. 2a,c, Extended Data Figs. 2,3 and 6, and Extended Data Table 1). The first state, which was resolved at 2.63 Å, is nearly identical to the choline-bound structure (all-atom RMSD 0.3 Å) (Extended Data Fig. 6). Indeed, inspection of the substrate-binding site reveals that it is occupied by a non-protein density that matches the choline density that we resolved in the choline-bound state (Fig. 2a–b). Based on the overall similarity of these structures, as well as the similarity of their substrate-binding sites, we assigned the density as a bound choline. As no choline was added during the purification, the bound choline must have been purified along with the transporter, indicating that choline binds to the substrate-binding site of FLVCR1 with high affinity.

The second state, which was resolved at 2.42 Å, also adopts an inward-facing state, but its conformation differs from the choline-bound states (Fig. 2c,e). The most pronounced difference is a tilt in TM8 that results in a slight displacement of its cytosolic end, with Gly381 and Gly384 serving as the pivots (Fig 2e). Within the substrate-binding site we observe a non-protein density corresponding to a bound ligand. The density occupying the substrate-binding site is too large to correspond to choline, and too small to correspond to heme, which has been previously proposed to be a substrate of FLVCR1[33] (Fig. 2d). As we are unable to determine the identity of this co-purified ligand, we assign this state as an endogenous ligand-bound state. Despite being occupied by a different ligand, the substrate-binding site of the endogenous ligand-bound state is very similar to that of the choline-bound state (Fig. 2f).

To generate hypotheses for additional substrates of FLVCR1, we used the Cancer Dependency Map (DepMap) project CRISPR 23Q2 public + score database[34] to identify genes that display co-essentiality with *FLVCR1*, as genes involved in the same metabolic pathways commonly exhibit similar patterns of essentiality[35,36]. Consistent with our previous report that *FLVCR1* serves a central role in choline metabolism[11], the gene with the second strongest association with *FLVCR1* was *CHKA* (Pearson correlation = 0.48), which encodes choline kinase alpha that catalyzes the first step of the choline branch of the Kennedy pathway[34] (Fig. 3a–b). Notably, the gene with the strongest association with *FLVCR1* was *ETNK1* (Pearson correlation = 0.51), which encodes ethanolamine kinase 1 that catalyzes the first step in the ethanolamine branch of the Kennedy pathway. Moreover, an association could also be identified between *FLVCR1* and *PCYT2* (Pearson correlation = 0.27), which encodes CTP:phosphoethanolamine cytidylyltransferase that catalyzes the second step of the ethanolamine branch of the Kennedy pathway. Although ethanolamine

kinase 1 and CTP:phosphoethanolamine cytidylyltransferase are not absolutely specific for the ethanolamine branch of the Kennedy pathway[37,38], these genetic associations suggest that in addition to its role in acquiring choline for the entry into the Kennedy pathway, FLVCR1 may also contribute to ethanolamine branch of the Kennedy pathway.

FLVCR1 is an ethanolamine transporter

To determine if FLVCR1 can transport ethanolamine, we compared the uptake of radiolabeled ethanolamine (ethanolamine [1-^{3}H] hydrochloride) between HEK293T cells and *FLVCR1*-knockout HEK293T cells over the course of 30 minutes. Strikingly, the ability to take up ethanolamine dropped by 93% following FLVCR1 deletion, suggesting that FLVCR1 is the major route for ethanolamine uptake in this cell type (Fig. 3c). This decline in ethanolamine uptake was comparable—or even greater than—the impact of FLVCR1 deletion on the uptake of radiolabeled choline in the same cells (Fig. 3f). Furthermore, re-expression of *FLVCR1* cDNA in the *FLVCR1*-knockout cells fully restored uptake of both choline and ethanolamine into cells, confirming that FLVCR1 expression is limiting for ethanolamine and choline uptake in cultured cells (Fig. 3c,d,f,g). When we compared choline and ethanolamine uptake, we found that ethanolamine was the preferred substrate of FLVCR1, with a K_m of 2.8 μM compared with a K_m of 8.0 μM for choline (Fig. 3e,h). Notably, the affinities that FLVCR1 displays for its substrates are very similar to the concentrations of ethanolamine (~2 μM) and choline (~10 μM) in plasma[2,23–26], indicating that FLVCR1 can serve as a high-affinity choline and ethanolamine transporter.

To determine how FLVCR1 recognizes and transports ethanolamine, we next collected cryo-EM images of FLVCR1 in the presence of 1 mM ethanolamine. Following several rounds of classification, we resolved two inward-facing states at resolutions of 2.50 and 3.02 Å (Extended Data Figs. 2,3 and 7, Extended Data Table 1). The two states are highly similar, with TM8 adopting the straight conformation that we had observed in the choline-bound states (Extended Data Fig. 7). Indeed, the only remarkable differences between the two states determined in the presence of ethanolamine are the shapes of the densities occupying the substrate-binding site (Fig. 3i–k and Extended Data Fig. 7). In the lower-resolution reconstruction, the substrate-binding site density overlaps with the choline densities resolved in the choline-bound states, indicating that this state may represent another endogenous choline-bound state (Extended Data Fig. 7). Although the limited resolution precludes definitive assignment of the substrate, this structure suggests that high concentrations of ethanolamine may be insufficient to completely compete away endogenous choline from the substrate-binding site.

The substrate-binding site density of the higher-resolution reconstruction is smaller and well accommodates an ethanolamine molecule (Fig. 3i). We therefore assigned this as an ethanolamine-bound state. Despite binding to a common site and not altering the global conformation of the transporter, ethanolamine interacts differently with FLVCR1 than does choline (Fig. 3j–k and Extended Data Fig. 7). Compared to choline, the primary amine of ethanolamine is shifted by 1.3 Å within the substrate-binding pocket towards TM2. The shift positions ethanolamine deeper within in the aromatic pocket formed by Trp125, Tyr153 and Tyr349 whereas the quaternary amine of the larger choline is partially outside

of the aromatic pocket. In addition to forming cation-π interactions with Trp125 and Tyr349 that are similar to those formed by choline, the deeper positioning of ethanolamine in the aromatic pocket enables its primary amine to interact with the side chain of Gln214, which is too far away to directly interact with the quaternary amine of choline. While we observe differential interactions between Gln214 and the amines of choline and ethanolamine, the hydroxyl groups of both substrates interact with Gln214 in a similar manner. Thus, the structures indicate that Gln214 serves a uniquely critical role in ethanolamine recognition by interacting with both its primary amine and its hydroxyl.

Specificity of the substate-binding site

Although choline and ethanolamine can occupy a common substrate-binding site, they interact differently with FLVCR1 in the inward-facing state. To assess the role of these differential interactions on transport, we mutated Trp125, Tyr153, Gln214, Asn245, Tyr349 and Gln471 in the substrate-binding pocket to alanine, expressed the mutants in *FLVCR1*-knockout cells and measured uptake of radiolabeled ethanolamine or radiolabeled choline after 30 minutes. The W125A mutant reduced uptake of both ethanolamine and choline to the levels similar to those of the *FLVCR1*-knockout cells, indicating that Trp125 is essential for metabolite transport (Fig. 4a–b and Extended Data Fig. 8). The Y153A and Y349A mutants also greatly diminished the transport of ethanolamine and choline, indicating that the aromatic residues that comprise the substrate-binding site are all critical for transport. Notably, the reduction in ethanolamine uptake caused by the Y349A mutant was greater than the effect on choline uptake, consistent with ethanolamine being more deeply embedded in the aromatic pocket of the substrate-binding site than choline. The Q214A mutant had an even more striking effect on transporter, with ethanolamine uptake being reduced by 94% compared to the wild-type transporter while choline uptake was unchanged. Mutation of the other two polar residues in the substrate-binding site, Asn245 and Gln471, had lesser effects on metabolite uptake, with the N245A mutant being slightly more severe. Thus, Gln214 is critical for ethanolamine but not choline uptake. We propose that the unique requirement of Gln214 for ethanolamine uptake results from Gln214 interacting with the charged primary amine of ethanolamine, but not with the charged quaternary amine of choline. Collectively, these data demonstrate that although FLVCR1 transports ethanolamine and choline via a common pathway, the interactions that stabilize these metabolites differ due to their unique chemical properties.

We next examined whether ethanolamine and choline transport by FLVCR1 contributes to both branches of the Kennedy pathway in cells. We performed metabolite isotope tracing experiments using isotopically labeled choline ([1,2-$^{13}C_2$] choline) or isotopically labeled ethanolamine ([1,2-$^{13}C_2$] ethanolamine) in *FLVCR1*-knockout cells and those expressing wild-type and mutant *FLVCR1* (Fig. 4c–f and Extended Data Fig. 8). Consistent with our previous finding that *FLVCR1* is critical for the choline branch of the Kennedy pathway[11], cells lacking *FLVCR1* displayed a 99% reduction in the incorporation of labeled choline into phosphocholine or the downstream metabolite betaine compared to the parental cells (Fig. 4f and Extended Data Fig. 9). Similarly, the loss of *FLVCR1* severely blunted the incorporation of labeled ethanolamine into phosphoethanolamine (Fig. 4e). The defects in incorporation of both choline and ethanolamine into downstream metabolites were specific

to *FLVCR1* as they could be rescued by expression of the *FLVCR1* cDNA, but not the W125A loss-of-function mutant (Fig. 4e–f). Consistent with the specific requirement of Gln214 for ethanolamine transport by FLVCR1, incorporation of ethanolamine into phosphoethanolamine could not be rescued by the Q214A mutant, although the Q214A mutant was sufficient to rescue the incorporation of choline into phosphocholine and betaine. The Y153A mutant, which reduced uptake of both radiolabeled choline and radiolabeled ethanolamine into cells, reduced incorporation of choline into phosphocholine and betaine, and ethanolamine into phosphoethanolamine, with the effect being stronger towards ethanolamine incorporation into ethanolamine. Consistent with our previous findings[39], *FLVCR1*-knockout cells grew slightly more slowly than *FLVCR1*-knockout cells expressing WT *FLVCR1* cDNA (Extended Data Fig. 8). *FLVCR1*-knockout cells expressing either the W125A or Y153A mutants, which cannot efficiently transport choline or ethanolamine, showed a similar reduction in growth rate. In contrast, *FLVCR1*-knockout cells expressing the Q214A, which only displays defects in ethanolamine transport, were indistinguishable from those expressing wild-type FLVCR1. Thus, FLVCR1 is a choline and ethanolamine transporter that is responsible for their uptake to fuel both branches of the Kennedy pathway.

Discussion

Phospholipid biosynthesis by the Kennedy pathway provides the phosphatidylcholine and phosphatidylethanolamine lipids that are essential for cellular proliferation. Here, we show that FLVCR1 is a transporter that serves as the common entry point for their biosynthesis, transporting extracellular choline and ethanolamine into the cytosol where they can be phosphorylated by choline kinase alpha and ethanolamine kinase 1, the enzymes that catalyze the first branches of the choline and ethanolamine branches of the Kennedy pathway, respectively (Fig. 4g). In contrast to other putative mammalian ethanolamine transporters, such as CTL1 and CTL2, which have affinities that are far below the ~2 μM ethanolamine circulating concentration in the plasma[2,40], the 2.8 μM K_m FLVCR1 that displays for ethanolamine is sufficiently high to enable its uptake into cells under physiological conditions. Notably, the K_m of FLVCR1 for choline (8.0 μM) is also similar to the circulating concentration of choline in blood plasma (~10 μM) [23–26], indicating that FLVCR1 can take up choline at physiological concentrations. With FLVCR1 having affinities that are so close to the physiological concentrations of choline and ethanolamine, it is likely that these two metabolites compete to bind FLVCR1.

A negative resting membrane potential favors the import of positively charged choline and ethanolamine into cells. Choline and ethanolamine import are also favored by the activities of choline kinase alpha and ethanolamine kinase 1, which ensure that cytosolic concentrations of ethanolamine and choline remain sufficiently low that there is a stable concentration gradient to drive their uptake from the extracellular space, a mechanism that is analogous to the uptake of sugars by the related GLUTs[41].

FLVCR1 is a member of the ubiquitous MFS family of membrane transporters that utilize a conserved rocker-switch alternating access transport mechanism to move substrates across membranes[16]. When bound by choline or ethanolamine, FLVCR1 adopts similar inward-

facing conformations that likely correspond to pre-release steps in the transport cycle. Notably, choline can co-purify with the transporter in these conformations, even when an ethanolamine is present at high concentrations for 30 minutes. An additional compound or compounds was also found to co-purify with FLVCR1 that stabilize a slightly different inward-facing state in which the central cavity is expanded, indicating that FLVCR1 can bind to multiple substrates and that these substrates can stabilize distinct states. Future studies will be needed to uncover the mechanisms of substrate release, which may require local or global conformational changes.

Despite binding to a common site, ethanolamine and choline interact differently with FLVCR1. Notably, Gln214 is required for ethanolamine transport, but not for choline transport. Tyr349 is also more important for uptake of ethanolamine than for choline. Future mutagenesis studies may uncover additional residues that can bias the substrate profile of the transporter. We recently demonstrated that the loss of FLVCR1 in mice leads to significant defects in mitochondrial metabolism and embryonic lethality around day E12.5, demonstrating that choline and/or ethanolamine transport by FLVCR1 for use in the Kennedy pathway is essential for mammalian viability[11]. Exploring the effects of mutations that alter the substrate profile of *FLVCR1* in cells and animals will enable a more complete understanding of the distinct physiological roles of ethanolamine and choline. Moreover, combining these substrate-specific mutations with variants in *FLVCR1* that lead to PCARP or variants in *FLVCR2* that lead to Fowler syndrome, all of which are located outside of the substrate-binding site, may aid in understanding the molecular basis of disease (Extended Data Fig. 5)[7,8,13].

Methods

Protein expression and purification

The gene encoding human FLVCR1 (hFLVCR1) was synthesized by Twist Biosciences and subcloned into a BacMam expression vector with a C-terminal mCerulean-tag fused via a short linker containing a PreScission protease site[42]. The plasmid was mixed 1:3 (w/w) with PEI 25 K (Polysciences, 23966-1) for 20 min at room temperature and then used to transfect HEK293S GnTi^{-} cells at 37 °C in 5% CO_2 (ATCC, CRL-3022). For a 1 L cell culture, 1 mg plasmid and 3 mg PEI 25 K were used. After 24 hr incubation at 37° C, valproic acid sodium salt (Sigma-Aldrich, P4543) was added to a final concentration of 2.2 mM, and cells were allowed to grow at 37 °C for an additional 48 hr before harvesting. Cell pellets were washed in phosphate-buffered saline solution and flash frozen in liquid nitrogen. For Cryo-EM analysis, the expressed protein was solubilized in 2 % lauryl maltose neopentyl glycol (LMNG) (Anatrace, NG310), 0.2 % Cholesteryl Hemisuccinate Tris Salt (CHS) (Anatrace, CH210), 20 mM HEPES (pHed with KOH, pH 7.5), 150 mM KCl supplemented with protease-inhibitor cocktail (1 mM PMSF, 2.5 mg/mL aprotinin, 2.5 mg/mL leupeptin, 1 mg/mL pepstatin A) and DNase I. For proteoliposome reconstitution, the expressed protein was solubilized in 2 % n-Dodecyl-β-D-Maltoside (DDM) (Anatrace, D310), 20 mM HEPES (pHed with KOH, pH 7.5), 150 mM KCl supplemented with protease-inhibitor cocktail (1 mM PMSF, 2.5 mg/mL aprotinin, 2.5 mg/mL leupeptin, 1 mg/mL pepstatin A) and DNase I. Solubilized proteins were separated by centrifugation 135,557 g for 50 min,

followed by binding to anti-GFP nanobody resin for 3 hr. Anti-GFP nanobody affinity chromatography was performed by 3 column volumes of washing with Size Exclusion Chromatography (SEC) buffer followed by overnight PreScission digestion and elution with SEC buffer. SEC buffer for Cryo-EM analysis consisted of 0.01 % LMNG, 0.001 % CHS, 20 mM HEPES (pHed with KOH, pH 7.5), and 150 mM KCl. The SEC buffer for proteoliposome reconstitution consisted of 0.34 mM DDM, 20 mM HEPES (pHed with KOH, pH 7.5), and 150 mM KCl. The eluted protein sample was concentrated to a volume of 250 μl using CORNING SPIN-X concentrators (50 kDa cutoff) (Corning, 431490), followed by centrifugation 21,130 g for 15 min. Concentrated protein was further purified by size exclusion chromatography on a Superdex 200 Increase 10/300 GL (GE healthcare, GE28-9909-44) in SEC buffer. For proteoliposome reconstitution, the peak fractions were pooled and used for proteoloiposome reconstitution immediately. For Cryo-EM analysis, peak fractions were pooled, mixed, and split into two samples in equal volume, of which one was incubated with choline chloride (Sigma-Aldrich, C7527) at a final concentration of 1 mM for 30 min on ice before concentrating to a protein concentration of 6 mg/ml, while the other was concentrated to a protein concentration of 6mg/ml without incubating with a ligand. Another hFLVCR1 expression and purification experiment was performed with identical procedures up to the size exclusion chromatography step, in which the SEC peak fractions were pooled, mixed, and incubated with ethanolamine (Sigma-Adrich, 398136) at a final concentration of 1 mM for 30 min on ice before concentrating to a protein concentration of 6 mg/ml.

Electron microscopy sample preparation and data acquisition

3 μl of 6 mg/ml purified hFLVCR1 with incubated for 30 minutes with 1 mM choline chloride, or with ethanolamine chloride, or without exogenous substrate was applied to glow-discharged Au 400 mesh QUANTIFOIL R1.2/1.3 holey carbon grids (Quantifoil) and then plunged into liquid nitrogen-cooled liquid ethane with an FEI Vitrobot Mark IV (FEI Thermo Fisher). The sample was frozen at 4 °C with 100 % humidity, using blotting times of 3.5 s to 4.5 s, blotting force of 0, and a waiting time of 10 s. Grids were either transferred to a 300 keV FEI Titan Krios microscopy equipped with a K3 summit direct electron detector (Gatan) or with a Falcon IV direct detector and a SeletrisX energy filter (ThermoFisher Scientific).

For images collected using a Gatan K3, the images were recorded with SerialEM[43] in super-resolution mode at 29,000×, corresponding to super-resolution pixel size of 0.413 Å. Dose rate was 15 electrons/pixel/s, and the defocus range was −0.5 to −1.5 μm. Images were recorded for 3 s with 0.05 s subframes (total 60 subframes), corresponding to a total dose of 66 electrons/Å.

For images collected with a Falcon IV, the images were recorded with Leginon[44] in pixel size of 0.725 Å. Dose rate was 5.67 electrons/pixel/s, and the defocus range was −0.5 to −1.5 μm. Images were recorded for 5 s with frame time of 0.003125 s, corresponding to a total dose of 53.98 electrons/ Å .

Electron microscopy data processing

Substrate-free sample—5700 of sixty-frame super-resolution movies (0.413 Å/pixel) of hFLVCR1 without substrate incubation were collected using K3 summit direct electron detector (Gatan). The movies were gain corrected, Fourier cropped by two (0.826 Å/pixel) and aligned using whole-frame and local motion correction algorithms by cryoSPARC v3.2.0[45]. Blob-based autopicking in cryoSPARC v3.2.0 was implemented to select initial particle images, resulting in 5,926,467 particles[45]. Several rounds of 2D classification were performed and the best 2D classes were manually selected to generate the initial 3D model using the ab initio algorithm in cryoSPARC v3.2.0[45]. False-positive selections and contaminants were excluded through iterative rounds of heterogeneous classification using the model generated from the ab initio algorithm as well as several decoy classes generated from noise particles via ab initio reconstruction in cryoSPARC v3.2.0[45], resulting in a stack of 2,709,623 particles. Then, 3D classification in cryoSPARC v3.2.0 [46] was performed using a focus mask that covers the FLVCR1 density but excludes the detergent micelle density, which we refer to as a FLVCR1 focus mask. The 3D classification did not resolve different conformations but separated the best-aligning particles from the rest of the particles that were seemingly in the same conformation, resulting in a stack of 824,310 best-aligning particles that yielded an improved reconstruction. After Bayesian polishing in Relion 3.1.2[47], the polished particle stacks were refined using non-uniform refinement in cryoSPARC v3.2.0 with global CTF estimation, as well as higher order tetrafoil, anisotropic magnification, and aberration corrections, yielding a reconstruction of 2.80 Å. The particles were then classified via 3D classification in cryoSPARC v3.2.0 using the FLVCR1 focus mask[46]. The 3D classification did not resolve different conformations but separated the best-aligning particles from rest of the particles that were seemingly in the same conformation. The final reconstruction of 265,053 particles at resolution 2.66 Å was used for a reference for heterogenous classifications of other datasets described below.

Choline sample—3988 of one-thousand-six-hundred-frame movies of hFLVCR1 incubated with choline chloride were collected using a Falcon IV direct detector with a SelectrisX energy filter (ThermoFisher Scientific). The movies were up-sampled by 2, fractionated to 40, and aligned using whole-frame and local motion correction algorithms by cryoSPARC v4.2.1[45]. Blob-based autopicking in cryoSPARC was implemented to select initial particle images, resulting in 2,712,047 particles. False-positive selections and contaminants were excluded through iterative rounds of heterogeneous classification using the final reconstruction obtained from the substrate-free dataset collected with the Gatan K3 detector, as well as several decoy classes generated from noise particles via ab initio reconstruction in cryoSPARC v4.2.1[45], resulting in a stack of 632,179 particles. After particle polishing in Relion 4.0.0[47] with up-sampling factor of 2 and fractionation of 40, the particles were subjected to non-uniform refinement in cryoSPARC v4.2.1 with global CTF estimation as well as higher order tetrafoil, anisotropic magnification, and aberration corrections in cryoSPARC v4.2.1. The refined particles were then classified via 3D classification in cryoSPARC v4.2.1 using the FLVCR1 focus mask without additional angular alignment[46]. The 3D classification did not resolve different conformations but separated the best-aligning particles that adopted a single conformation. A non-uniform refinement followed by local-refinement of the subsequent 290,450 particles in cryoSPARC

v4.2.1[45] achieved a resolution of 2.60 Å. The final reconstruction was subjected to density modification using the two unfiltered half-maps with a soft mask in Phenix[48], yielding an improved density map at 2.52 Å that we call choline-bound hFLVCR1. The density modified map was then used to build the choline-bound hFLVCR1 structure.

Substrate-free sample—9694 of one-thousand-six-hundred-frame movies of hFLVCR1 without substrate incubation were collected from two grids using a Falcon IV direct detector with a SelectrisX energy filter (ThermoFisher Scientific). The movies were up-sampled by 2, fractionated to 40, and aligned using whole-frame and local motion correction algorithms in cryoSPARC v4.2.1[45]. Blob-based autopicking in cryoSPARC was implemented to select initial particle images, resulting in stacks of 3,374,453 and 3,166,447 particles. False-positive selections and contaminants were excluded through iterative rounds of heterogeneous classification using the final reconstruction obtained from the substrate-free dataset collected with K3 summit direct electron detector, as well as several decoy classes generated from noise particles via ab initio reconstruction in cryoSPARC v4.2.1[45], resulting in stacks of 661,859 and 515,821 particles. After particle polishing in Relion 4.0.0.[47], the stacks were subjected to non-uniform refinement in cryoSPARC v4.2.1 with global CTF estimation as well as higher order tetrafoil, anisotropic magnification, and aberration corrections in cryoSPARC v4.2.1. The two stacks were then classified via 3D classification in cryoSPARC v4.2.1[46] using the FLVCR1 focus mask without additional angular alignment. Two classes of particles in distinct conformations were identified after the 3D classification. A non-uniform refinement followed by local refinement of one of the two classes resulted in reconstruction of 50,496 particles at 2.63 Å. Density modification of the first state using the two unfiltered half-maps with a soft mask in Phenix[48] yielded an improved density map at 2.60 Å in which clear density for a choline was observed in the in the substrate-binding site and thus we call the endogenous choline-bound FLVCR1. A non-uniform refinement of the second class resulted in a reconstruction of 193,986 particles at 2.42 Å. Density modification of the second map using the two unfiltered half-maps with a soft mask in Phenix[48] yielded an improved density map at 2.38 Å. Inspection of the second map revealed the presence of a density in the cavity that does not correspond to choline and we thus call this map the endogenous ligand-bound FLVCR1.

Ethanolamine sample—3675 of sixty-frame super-resolution movies (0.413 Å/pixel) of hFLVCR1 incubated with ethanolamine were collected using K3 summit direct electron detector (Gatan). The movies were gain corrected, Fourier cropped by two (0.826 Å/pixel) and aligned using whole-frame and local motion correction algorithms by cryoSPARC v3.2.0[45]. Blob-based autopicking in cryoSPARC v3.2.0 was implemented to select initial particle images, resulting in 5,046,088 particles[45]. False-positive selections and contaminants were excluded through iterative rounds of heterogeneous classification using the final reconstruction obtained from the substrate-free dataset collected with the Gatan K3 detector, as well as several decoy classes generated from noise particles via ab initio reconstruction in cryoSPARC v4.2.1[45], resulting in a stack of 756,224 particles. Following non-uniform reconstruction, the particles were then classified via 3D classification[46] in cryoSPARC v4.2.1 using the FLVCR1 focus mask. The 3D classification did not resolve different conformations but separated the best-aligning particles that adopted a single

conformation. A non-uniform refinement of the subsequent 370,203 particles in cryoSPARC v4.2.1[45] achieved a resolution of 2.74 Å. After Bayesian polishing in Relion 3.1.2[47], the polished particle stacks were refined using non-uniform refinement in cryoSPARC v3.2.0 with global CTF estimation, yielding a reconstruction of 2.65 Å. The refined particles were then classified via 3D classification in cryoSPARC v3.2.0 using the FLVCR1 focus mask[46] without additional angular alignment[46]. Two classes of particles in distinct conformations were identified after the 3D classification. A non-uniform refinement of one of the two classes resulted in reconstruction of 36,781 particles at 3.02 Å that is equivalent to the choline-bound hFLVCR1 density map obtained from the movies of hFLVCR1 incubated with choline chloride collected with Falcon IV detector. A non-uniform refinement of the second class followed by local-refinement resulted in a reconstruction of 119,001 particles at 2.50 Å. Density modification of the first map using the two unfiltered half-maps with a soft mask in Phenix[48] yielded an improved density map at 2.93 Å in which density corresponding to a bound choline could be observed in the substrate-binding site. Density modification of the second map using the two unfiltered half-maps with a soft mask in Phenix[48] yielded an improved density map at 2.49 Å. Inspection of the map revealed the presence of a bound ethanolamine and we thus call this map the ethanolamine-bound FLVCR1.

Model building and coordinate refinement

The structure of hFLVCR1 was automatically built into the choline-bound hFLVCR1 density map using ModelAngelo[49]. Densities corresponding to N- and C-terminus loops consisting of residues 1-98 and 517-555, respectively, were too poorly ordered and omitted from the model. The choline-bound hFLVCR1 model contains residues 99-516. The models were then manually rebuilt using COOT[50] to fit the density. Choline and water molecules were modelled into non-protein density peaks using local geometry and a minimum threshold of 10.0 sigma in the density-modified and sharpened map. Atomic coordinates were refined against the density modified map using phenix.real_space_refinement with geometric and Ramachandran restraints maintained throughout [51].

The choline-bound model was docked into the endogenous choline map obtained from substrate-free sample using Chimera[52]. The model was then manually rebuilt using COOT [50] to fit the density. Densities corresponding to N- and C-terminus loops consisting of residues 1-98 and 518-555, respectively, were too poorly ordered and omitted from the model. The water molecules were modelled into non-protein density peaks using local geometry and a minimum threshold of 13.0 sigma in the density-modified and sharpened map. Atomic coordinates were refined against the density modified map using phenix.real_space_refinement with geometric and Ramachandran restraints maintained throughout.

The structure of unknown endogenous ligand-bound hFLVCR1 was initially built into the endogenous ligand-bound hFLVCR1 density map using ModelAngelo[49]. Densities corresponding to N- and C-terminus loops consisting of residues 1-96 and 519-555, respectively, were too poorly ordered and omitted from the model. The unknown endogenous ligand-bound hFLVCR1 model contains residues 97-518. The models were then

manually rebuilt using COOT[50] to fit the density. Ethanolamine and water molecules were modelled into non-protein density peaks using local geometry and a minimum threshold of 10.0 sigma in the density-modified and sharpened map. Atomic coordinates were refined against the density modified map using phenix.real_space_refinement with geometric and Ramachandran restraints maintained throughout [51].

The choline-bound model was docked into the ethanolamine-bound map using Chimera [52]. Densities corresponding to N- and C-terminus loops consisting of residues 1-96 and 516-555, respectively, were too poorly ordered and omitted from the model. The ethanolamine-bound hFLVCR1 model contains residues 97-515. The model was then manually rebuilt using COOT [50] to fit the density. The ethanolamine and water molecules were modelled into non-protein density peaks using local geometry and a minimum threshold of 6.7 sigma in the density-modified and sharpened map. Atomic coordinates were refined against the density modified map using phenix.real_space_refinement with geometric and Ramachandran restraints maintained throughout.

The choline-bound model was docked into the endogenous choline map obtained from ethanolamine-incubated sample using Chimera[52]. Densities corresponding to N- and C-terminus loops consisting of residues 1-98 and 514-555, respectively, were too poorly ordered and omitted from the model. The ethanolamine-bound hFLVCR1 model contains residues 99-513. The model was then manually rebuilt using COOT[50] to fit the density. The ethanolamine and water molecules were modelled into non-protein density peaks using local geometry and a minimum threshold of 8.0 sigma in the density-modified and sharpened map. Atomic coordinates were refined against the density modified map using phenix.real_space_refinement with geometric and Ramachandran restraints maintained throughout [51].

Fluorescence size exclusion chromatography (FSEC)

Mutant hFLVCR1 constructs were generated via PCR using the WT hFLVCR1 construct, the primers listed in ‘Oligonucleotide sequences’ (synthesized by IDT) and Q5 polymerase (New England Biolabs, Q5 high fidelity 2X master mix M0492S), followed by HiFi-DNA assembly (New England Biolabs, E2621L) using the BacMam vector[42] linearized with XhoI and EcoRI. All construct sequences were validated by Sanger sequencing.

FLVCR1-knockout HEK293T cells[11] were seeded at a concentration of 500,000 cells per 6-well plate. The following day, the plasmid encoding mCerulean-tagged WT or mutant hFLVCR1 was mixed 1:3 (w/w) with PEI 25 k (Polysciences, Inc) for 20 min at room temperature and then used to transfect the *FLVCR1*-knockout HEK293T cells. After 24 hr incubation at 37 °C, valproic acid sodium salt (Sigma-Aldrich, P4543) was added to a final concentration of 2.2 mM, and cells were allowed to grow at 37 °C for an additional 48 hr before harvesting. Cell pellets were washed in phosphate-buffered saline solution and flash frozen in liquid nitrogen. Expressed proteins were solubilized in 2 % n-Dodecyl-β-D-maltoside (DDM) (Anatrace, D310), 20 mM HEPES pH 7.5 (pHed with KOH, pH 7.5), 150 mM KCl supplemented with protease-inhibitor cocktail (1 mM PMSF, 2.5 mg/mL aprotinin, 2.5 mg/mL leupeptin, 1 mg/mL pepstatin A) and DNase I (Worthington Biochemical, LS002139). Solubilized proteins were separated by centrifugation 15,871 g for

45 min. Separated proteins were injected to and monitored by fluorescence size exclusion chromatography on a Superose 6 Increase 10/300 GL (GE healthcare, GE29-0915-96) in a buffer composed of 1 mM DDM, 150 mM KCl, 20 mM HEPES pH 7.5 (pHed with KOH, pH 7.5). Fluorescence was monitored at 433/475 nm for excitation/emission wavelength, respectively.

Generation of stable cell lines—Genes encoding WT or mutant hFLVCR1 in the BacMam vector[42] were subcloned into pMXS-IRES-BLAST (Cell Biolabs, RTV-016) linearized with BamHI and NotI using Gibson Assembly (New England Biolabs, E2611) [11] using another set of primers listed in "Oligonucleotide sequences." All construct sequences were validated by Sanger Sequencing. The cDNA expressing vectors along with retroviral packaging vectors Gag-Pol and VSG-G were transfected into HEK293T cells using X-tremeGENE 9 DNA Transfection reagent (Roche, 6364787001). Virus-containing supernatant was collected 48 hr after transfection and passed through a 0.45 μm filter. *FLVCR1*-knockout HEK293T cells[11] in 6-well tissue culture plates were spin-infected with virus and 4 μg/mL polybrene by centrifugation at 2,200 rpm for 80 min. Cells were selected by 20 μg/mL blasticidin (Invivogen, ant-bl-1). For all constructs the matching vector without insert was used as a control. All cell lines were grown in RPMI 1640 medium (Gibco, 11875-093) containing 2 mM glutamine supplemented with 10 % fetal bovine serum (FBS) and were maintained at 37 °C and 5 % CO2.

Cell-based radioactive substrate uptake experiments

Radioactive substrate uptake experiments were performed as in[11] unless otherwise stated. Briefly, cells were seeded in RPMI 1640 medium (Gibco, 11875-093) containing 2mM glutamine supplemented with 10 % fetal bovine serum (FBS) at 250,000 per mL or 500,000 cells per well in a 6-well plate in triplicate. The following day, media was aspirated and cells were incubated in room temperature Krebs-Ringer Buffer (Alfa Aesar, J67795) for 30 minutes. Cells were then incubated with indicated concentration of choline chloride or ethanolamine in room temperature Krebs-Ringer Buffer for timepoints described in figure legends. For all concentrations of choline chloride and ethanolamine, 0.093% of the total choline or ethanolamine concentration stated on figure legends was radioactive ([Methyl-^{3}H]-Choline Chloride; Perkin Elmer, NET109001MC; 73.7 Ci/mmol) (Choline chloride; Sigma-Aldrich, C7527) (ethanolamine [1-^{3}H] hydrochloride; American Radiolabeled Chemicals, ARC-0216A; 40.0 Ci/mmol) (ethanolamine; Sigma-Aldrich, 398136). For example, 20 nM was radioactive of total 21.5 μM choline used, and 1.86 nM was radioactive of total 2 μM ethanolamine used. Following incubation, cells were washed twice with ice cold Krebs-Ringer Buffer on ice. Cells were then solubilized with 200 μL of 1 % SDS 0.2 N NaOH and transferred to a scintillation vial with 10 mL of Insta-Gel Plus scintillation cocktail (Perkin Elmer, 601339). Radioactivity was measured with a liquid scintillation analyzer (Perkin Elmer, Tri-Carb 2910-TR). To determine K_m and V_{max}, the cells was incubated with indicated concentration of choline chloride or ethanolamine for 1 min at room temperature. The amount of choline uptake by *FLVCR1*-knockout HEK293T cells expressing a vector control was subtracted from the amount of choline uptake by *FLVCR1*-knockout HEK293T cells expressing *FLVCR1* cDNA. Michaelis-Menten model

was fitted to the data using GraphPad Prism (www.graphpad.com) to calculate K_m and V_{max}.

FLVCR1 Coessentiality Analysis

To perform a coessentiality mapping, we analyzed the DepMap 23Q2 Public+Score, Chronos dataset that contains the genetic perturbation scores of 1,095 cancer cell lines[34]. Specifically, we computed Pearson correlation values in a pairwise manner between the perturbation scores of FLVCR1 and 17,927 other genes present in the dataset. The code used to perform the analysis is available on Github (https://github.com/artemkhan/Coessentiality_DepMAP_FLVCR1.git).

Immunoblotting

Cells were lysed in RIPA buffer (Cell Signaling Technology, 9806S) supplemented with protease-inhibitor cocktail (1 mM PMSF, 2.5 mg/mL aprotinin, 2.5 mg/mL leupeptin, 1 mg/mL pepstatin A) and phosphatase inhibitor cocktail (Sigma-Aldrich, P0044). Lysates were centrifuged at 18,000 g for 10 min. Total protein was quantified using BCA Protein Assay Kit (Thermo Fisher, 23227) with provided albumin standard used as a protein standard. Samples were resolved on 4-12% Bis-Tris gels (Thermo Scientific, NW04125BOX) and analyzed by standard immunoblotting techniques. Briefly, gels were transferred in Transfer buffer (25 mM Tris base, 190 mM glycine, 20 % methanol, pH 8.3) to nitrocellulose membranes (Bio-Rad, 1620115) and incubated with primary antibodies (FLVCR, Santa Cruz Biotechnology sc-390100; GAPDH, Cell Signalling Technology 5174) at 4°C overnight. Secondary antibody incubation was performed at room temperature for 1 hr using anti-mouse IgG-HRP (Santa Cruz Biotechnology, sc-525408) and anti-rabbit IgG-HRP (Cell Signalling Technology #7074). Washes were performed with 0.1% Tween-20 tris buffered saline and blots developed using ECL western blotting detection reagents (Cytiva, RPN2209).

Isotope tracing

Polar metabolomics and isotope tracing experiments were performed as previously described[11]. Briefly, 250,000 cells were seeded per 6-well in triplicate per condition. For choline tracing experiments, cells were seeded in choline depleted medium and the next day changed to fresh choline depleted medium supplemented with 21.5 uM [1,2,-$^{13}C_2$]Choline chloride (Cambridge Isotope Laboratories, CLM-548.01). For ethanolamine tracing experiments, cells were seeded in RPMI 1640 medium (Gibco, 11875-093) with 2 mM glutamine supplemented with 10 % dialyzed fetal bovine serum (Gibco, 26400-044) and 1 % penicillin streptomycin and the next day changed to fresh medium with 2 uM [1,2,-$^{13}C^2$]ethanolamine hydrochloride (Cambridge Isotope Laboratories, CLM-274-0.1). For both choline and ethanolamine tracing, incubation was performed for 1 hour in a tissue culture incubator. Polar metabolites were extracted and analyzed by LC/MS as follows[11]. Metabolite peaks were picked from LC-MS data using Skyline Daily v22 with a 3ppm mass tolerance and a 6 second retention time from known standards run with all LC-MS experiments. As an internal standard for metabolite extraction and LC-MS injection volume the abundance of ^{15}N and ^{13}C fully-labeled amino acids was used to normalize reported metabolite levels. Further, reported metabolite levels were normalized to protein abundance

of cells in each condition. Reported M+2 metabolite levels include a theoretical correction for natural ^{13}C M+2 abundance relative to M+0 pool size.

Cell growth curves

HEK293T, HEK293T *FLVCR1* KO + WT *FLVCR1* cDNA, HEK293T *FLVCR1* KO + control vector, HEK293T *FLVCR1* KO + W125A *FLVCR1* cDNA, HEK293T *FLVCR1* KO + Y153A *FLVCR1* cDNA, and HEK293T *FLVCR1* KO + Q214A *FLVCR1* cDNA cells were plated in 6 well plates. 40,000 cells were seeded in triplicates. Cells were trypsinized and counted using a Beckman Coulter Multisizer 4e every 24 hr for four days, at which time the cells reached confluency. Cells were grown in RPMI 1640 medium (Gibco, 11875-093) containing 2 mM glutamine supplemented with 10 % fetal bovine serum (FBS) and were maintained at 37 °C and 5 % CO2.

Proteoliposome reconstitution

Lipids were prepared using 3:1 (w/w) ratio of 1-palmitoyl-2-oleoyl- *sn*-glycero-3-phosphoethanolamine (POPE) (Avanti Polar Lipids, 850757C), and 1-palmitoyl-2-oleoyl-sn-glycero-3-phospho-(1'-rac-glycerol) (sodium salt) (POPG) (Avanti Polar Lipids, 840457C). The lipids in chloroforms were dried under argon and then under vacuum overnight at room temperature. The lipids were rehydrated at 10 mg/ml in internal liposome buffer (20 mM HEPES, pH 7.5, 150mM KCl, 2 mM choline chloride (Sigma-Aldrich, C7527)) by incubating in 37°C shaker for 40 minutes. The lipid mixture was then sonicated until the mixture became lipid chunk-free and homogenous. The lipid suspension was subjected to 10 freeze-thaw cycles and was extruded 11 times through 400 nm polycarbonate membranes (Avanti Polar lipids, 10417104) using a syringe extruder (Avanti Polar lipids, 610000). Liposomes were destabilized with DDM at a final concentration of 0.34 mM for 1 hours at 4°C. hFLVCR1 was purified as described in the "protein expression and purification" method section. The purified hFLVCR1 was added to the destabilized lipids at a 1:500 (w/w) protein to lipid ratio for 2 hr at 4°C. For the control protein-free liposome reconstitution, equivalent volume of SEC buffer from protein purification step was added. The detergent removal was conducted by incubating the protein-lipid mixture with SM-2 bio-beads (Bio-rad, 1523920) at a 2:1 (v/v) protein-lipid mixture to bio-beads ratio at 4°C overnight, followed by additional bio-beads incubation at a 100:17 (v/v) protein-lipid mixture to bio-beads ratio at 4°C for 2 hrs. The proteoliposomes or control liposomes were concentrated to10 mg/ml lipid concentration by ultracentrifugation at 100,000g for 45 min at 4°C. The liposomes aliquots were flash-frozen with liquid nitrogen and stored at −80°C until use.

Proteoliposome uptake assay

Prior to proteoliposome uptake assay, the frozen proteoliposome aliquot was thawed and diluted by 10 fold in the internal liposome buffer. The proteoliposomes was then subjected to three freeze-thaw cycle and was extruded 11 times through 400 nm polycarbonate membranes (Avanti Polar lipids, 10417104) using a syringe extruder (Avanti Polar lipids, 610000). The proteoliposomes were concentrated to 10 mg/ml lipid concentration again by ultracentrifugation at 100,000g for 45 min at 4°C. The proteoliposomes were diluted by 10 fold in the reaction buffer and was incubated for timepoints described in the figure legends at room temperature. The proteoliposome solution was rapidly aspirated through 0.22 μm

membrane filters (Millipore, MSGVN2210) under vacuum to stop substrate uptake by proteoliposomes. The filters were washed three times with 4X volume of internal liposome buffer and transferred to a scintillation vial with 5 mL of Insta-Gel Plus scintillation cocktail (Perkin Elmer, 601339). Radioactivity was measured with a liquid scintillation analyzer (Perkin Elmer, Tri-Carb 2910-TR). Same procedures were conducted for the control protein-free liposomes.

For valinomycin experiment, the reaction buffer consisted of 152 mM NaCl, 20 mM HEPES (pH 7.5), 20 nM radioactive choline ([Methyl-^{3}H]-Choline Chloride; Perkin Elmer, NET109001MC; 73.7 Ci/mmol), and 1 mM valinomycin or equivalent volume of DMSO. For pH dependency experiment, the reaction buffer consisted of 150 mM KCl, 20 mM HEPES, and 20 nM radioactive choline ([Methyl-^{3}H]-Choline Chloride; Perkin Elmer, NET109001MC; 73.7 Ci/mmol). The pH was adjusted to 4.5-10.5 using KOH and HCl. For cation dependency experiment, reaction buffer in presence of potassium (150 mM KCl, 20 mM HEPES (pH 7.5), and 20 nM radioactive choline ([Methyl-^{3}H]-Choline Chloride; Perkin Elmer, NET109001MC; 73.7 Ci/mmol)), or sodium (150 mM NaCl, 20 mM HEPES (pH 7.5), and 20 nM radioactive choline ([Methyl-^{3}H]-Choline Chloride; Perkin Elmer, NET109001MC; 73.7 Ci/mmol)), or calcium (150 mM KCl, 20 mM HEPES (pH 7.5), 1 mM $CaCl_2$ and 20 nM radioactive choline ([Methyl-^{3}H]-Choline Chloride; Perkin Elmer, NET109001MC; 73.7 Ci/mmol)), or magnesium (150 mM KCl, 20 mM HEPES (pH 7.5), 1 mM $MgCl_2$ and 20 nM radioactive choline ([Methyl-^{3}H]-Choline Chloride; Perkin Elmer, NET109001MC; 73.7 Ci/mmol)) were used. For the pH dependency and cation dependency experiments, the amount of substrate uptake by the control protein-free liposomes was subtracted from that by the proteoliposomes, which was then divided by the amount of protein in proteoliposomes to calculate substrate uptake in pmol/mg of FLVCR1.

Statistics and Reproducibility

All error bars are represented as mean values ± the standard deviation. All tests for statistical significance were performed using two-tailed unpaired t-test in Graphpad prism. All metabolite uptake and labeling experiments were independently performed at least twice, the results being similar. Cellular growth assays were performed twice with similar results. Cryo-EM images were collected from 1-2 grids per sample condition. The number of collected images for each condition is indicated in Extended Data Figure 3.

Figures

Figures were prepared with PyMol 2.5.3. (www.pymol.org), ChimeraX 1.5 [53], CAVER 3 [54], GraphPad Prism 9 (www.graphpad.com), Clustal Omega 1.2.3.[55], and pyBoxshade (https://github.com/mdbaron42/pyBoxshade).

Oligonucleotide sequences

Primers used to clone from BacMam vector to pMXS-IRES-BLAST vector—5’ GGGCGGAATTTACGTAGCCTAGATAGCACTCTCAGATTGTTTACTC 3’

5’ GCCGGATCTAGCTAGTTAATTAAATGGCCCGCCCCG 3’

WT hFLVCR1

Forward primer used for cloning synthesized WT hFLVCR1 into BacMam expression vector—GCTAGCCTCGAGCCACCATGGCCCGCCCCGATGACGA

Reverse primer used for cloning synthesized WT hFLVCR1 into BacMam expression vector—TCCAAAGAATTCGAGATAGCACTCTCAGATTGTT

cDNA (Codon Optimized; 5’-3’)

ATGGCCCGCCCCGATGACGAAGAGGGAGCTGCCGTAGCTCCTGGCCATCCACTGG
CCAAGGGGTATCTGCCTCTCCCACGGGGTGCCCCTGTGGGAAAAGAATCCGTCG
AACTTCAAAATGGCCCTAAGGCCGGAACTTTTCCTGTTAACGGCGCGCCTCGTGA
TTCTCTGGCAGCTGCTAGCGGTGTATTGGGTGGACCACAAACCCCACTTGCACCC
GAAGAAGAAACACAAGCCAGATTGCTGCCAGCCGGCGCGGGCGCCGAAACCCCC
GGCGCCGAATCATCACCACTTCCTCTGACAGCCCTGTCTCCTAGACGATTTGTCGT
CCTGCTCATATTTAGTCTTTACTCTCTCGTGAACGCATTCCAATGGATACAGTATTC
AATAATCTCAAATGTGTTTGAAGGATTTTATGGCGTGACTCTGTTGCATATAGATTG
GCTTAGCATGGTCTATATGCTCGCTTATGTTCCTCTGATATTTCCAGCTACATGGCTT
CTCGATACTAGGGGTCTCCGCCTTACAGCACTCCTCGGGTCAGGTCTGAATTGTCT
CGGAGCATGGATAAAATGTGGATCCGTCCAACAACACCTGTTTTGGGTGACGATG
CTCGGGCAATGTCTTTGTTCAGTTGCACAAGTCTTTATTCTCGGGCTGCCATCAAG
AATTGCTTCTGTCTGGTTCGGCCCTAAGGAAGTAAGCACGGCCTGCGCAACGGCA
GTCCTTGGGAACCAACTTGGCACCGCTGTCGGGTTCCTGCTGCCACCCGTGCTGG
TGCCTAATACCCAAAACGATACGAACCTGCTCGCCTGCAACATTTCCACTATGTTC
TACGGCACCTCTGCAGTGGCGACTCTCCTGTTCATACTGACCGCGATCGCGTTCAA
GGAGAAGCCGCGCTACCCACCGTCACAAGCCCAGGCTGCCTTGCAGGATTCACC
ACCCGAGGAATATAGCTACAAGAAGAGCATCAGGAATTTGTTCAAGAATATCCCGT
TCGTGCTGTTGCTGATTACCTACGGCATTATGACAGGGGCATTTTATAGTGTGTCAA
CTCTCCTCAATCAAATGATTCTCACATATTATGAAGGTGAGGAAGTGAACGCAGGC
AGAATCGGCCTGACCCTTGTGGTCGCCGGCATGGTAGGTAGCATCCTGTGCGGTT
TGTGGCTCGACTACACCAAGACGTATAAGCAAACGACCCTTATTGTCTACATACTG
TCCTTCATCGGCATGGTCATTTTCACCTTTACTCTGGATCTGAGGTACATCATTATT
GTCTTCGTGACCGGTGGCGTCCTGGGGTTCTTTATGACAGGCTATCTGCCCCTGGG
GTTCGAGTTCGCCGTCGAGATTACATATCCCGAGTCAGAGGGGACATCTTCCGGG
CTGCTGAACGCAAGCGCCCAAATTTTCGGTATCCTGTTTACCCTGGCCCAGGGGA
AATTGACCTCTGATTACGGACCGAAAGCTGGTAATATCTTCCTTTGCGTGTGGATG
TTCATTGGGATTATCCTGACGGCCCTGATTAAATCCGACCTTCGGCGGCATAATATC
AACATTGGGATCACCAACGTCGACGTCAAGGCCATCCCCGCCGATAGCCCGACTG
ATCAGGAGCCTAAGACTGTGATGCTGAGTAAACAATCTGAGAGTGCTATCTAG

W125A hFLVCR1

Forward primer 1 (5’-3’)

GTCCGAAGCGCGCTAGC

Reverse primer 1 (5’-3’)

GAATACTGTATGGCTTGGAATGCGTTC

Forward primer 2 (5’-3’)

GAACGCATTCCAAGCCATACAGTATTC

Reverse primer 2 (5’-3’)

GGACCTTGAAACAAAACTTCCAAAGAATTCGAG

Q471A hFLVCR1

Forward primer 1 (5’-3’)

GTCCGAAGCGCGCTAGC

Reverse primer 1 (5’-3’)

CCGAAAATGGCGGCGCTTGCGTTC

Forward primer 2 (5’-3’)

GAACGCAAGCGCCGCCATTTTCGG

Reverse primer 2 (5’-3’)

GGACCTTGAAACAAAACTTCCAAAGAATTCGAG

Y349A hFLVCR1

Forward primer 1 (5’-3’)

GTCCGAAGCGCGCTAGC

Reverse primer 1 (5’-3’)

GTTGACACACTGGCAAATGCCCCTG

Forward primer 2 (5’-3’)

CAGGGGCATTTGCCAGTGTGTCAAC

Reverse primer 2 (5’-3’)

GGACCTTGAAACAAAACTTCCAAAGAATTCGAG

Q214A hFLVCR1

Forward primer 1 (5’-3’)

GTCCGAAGCGCGCTAGC

Reverse primer 1 (5’-3’)

CCGAGAATAAAGACGGCTGCAACTGAAC

Forward primer 2 (5’-3’)

GTTCAGTTGCAGCCGTCTTTATTCTCGG

Reverse primer 2 (5’-3’)

GGACCTTGAAACAAAACTTCCAAAGAATTCGAG

N245A hFLVCR1

Forward primer 1 (5’-3’)

GTCCGAAGCGCGCTAGC

Reverse primer 1 (5’-3’)

GTGCCAAGTTGGGCCCCAAGGACTG

Forward primer 2 (5’-3’)

CAGTCCTTGGGGCCCAACTTGGCAC

Reverse primer 2 (5’-3’)

GGACCTTGAAACAAAACTTCCAAAGAATTCGAG

Y153A hFLVCR1

Forward primer 1 (5’-3’)

GTCCGAAGCGCGCTAGC

Reverse primer 1 (5’-3’)

CATAAGCGAGCATGGCGACCATGCTAAG

Forward primer 2 (5’-3’)

CTTAGCATGGTCGCCATGCTCGCTTATG

Reverse primer 2 (5’-3’)

GGACCTTGAAACAAAACTTCCAAAGAATTCGAG

N121D hFLVCR1

Forward primer 1 (5’-3’)

GTCCGAAGCGCGCTAGC

Reverse primer 1 (5’-3’)

CATTGGAATGCGTCCACGAGAGAG

Forward primer 2 (5’-3’)

CTCTCTCGTGGACGCATTCCAATG

Reverse primer 2 (5’-3’)

GGACCTTGAAACAAAACTTCCAAAGAATTCGAG

C192R hFLVCR1

Forward primer 1 (5’-3’)

GTCCGAAGCGCGCTAGC

Reverse primer 1 (5’-3’)

GGACGGATCCCCGTTTTATCCATG

Forward primer 2 (5’-3’)

catggataaaaCGGgatccgtcc

Reverse primer 2 (5’-3’)

CATGGATAAAACGGGGATCCGTCC

N467A hFLVCR1

Forward primer 1 (5’-3’)

GTCCGAAGCGCGCTAGC

Reverse primer 1 (5’-3’)

GGGCGCTTGCGGCCAGCAGCCCGG

Forward primer 2 (5’-3’)

CCGGGCTGCTGGCCGCAAGCGCCC

Reverse primer 2 (5’-3’)

GGACCTTGAAACAAAACTTCCAAAGAATTCGAG

A241T hFLVCR1

Forward primer 1 (5’-3’)

GTCCGAAGCGCGCTAGC

Reverse primer 1 (5’-3’)

CCCAAGGACGGTCGTTGCGCAG

Forward primer 2 (5’-3’)

CTGCGCAACGACCGTCCTTGGG

Reverse primer 2 (5’-3’)

GGACCTTGAAACAAAACTTCCAAAGAATTCGAG

Extended Data

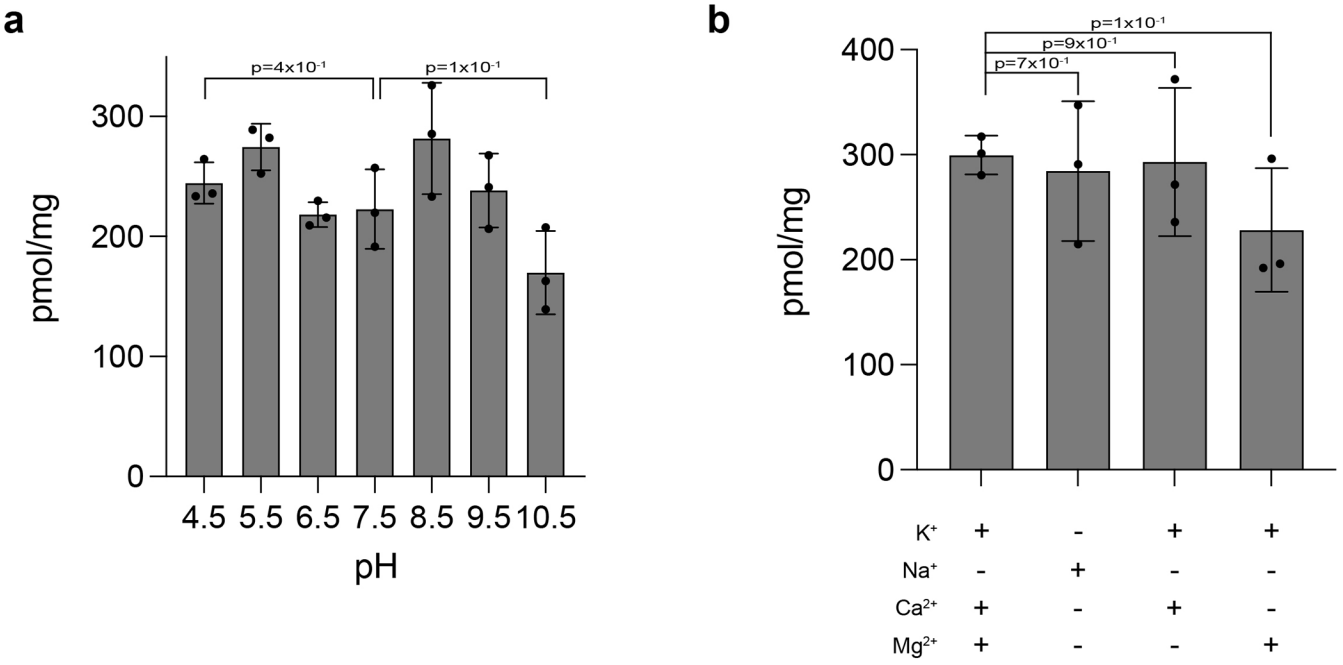

Extended Data Fig. 1: Regulation of FLVCR1-mediated choline uptake.

a, Background subtracted uptake of 20 nM [methyl-^{3}H]choline by vesicles containing FLVCR1 after 30 minutes in buffer at pH 4.5-10.5. Background was measured by uptake of 20 nM [methyl-^{3}H]choline into the protein-free control liposomes. n=3 technically independent samples. **b**, Background subtracted uptake of 20nM [methyl-^{3}H]choline by FLVCR1 proteoliposome after 30 minutes in buffer in the presence or absence of Na^+, K^+, Ca^{2+}, or Mg^{2+}. Background was measured by uptake of 20 nM [methyl-^{3}H]choline into the protein-free control liposomes. n=3 technically independent samples.

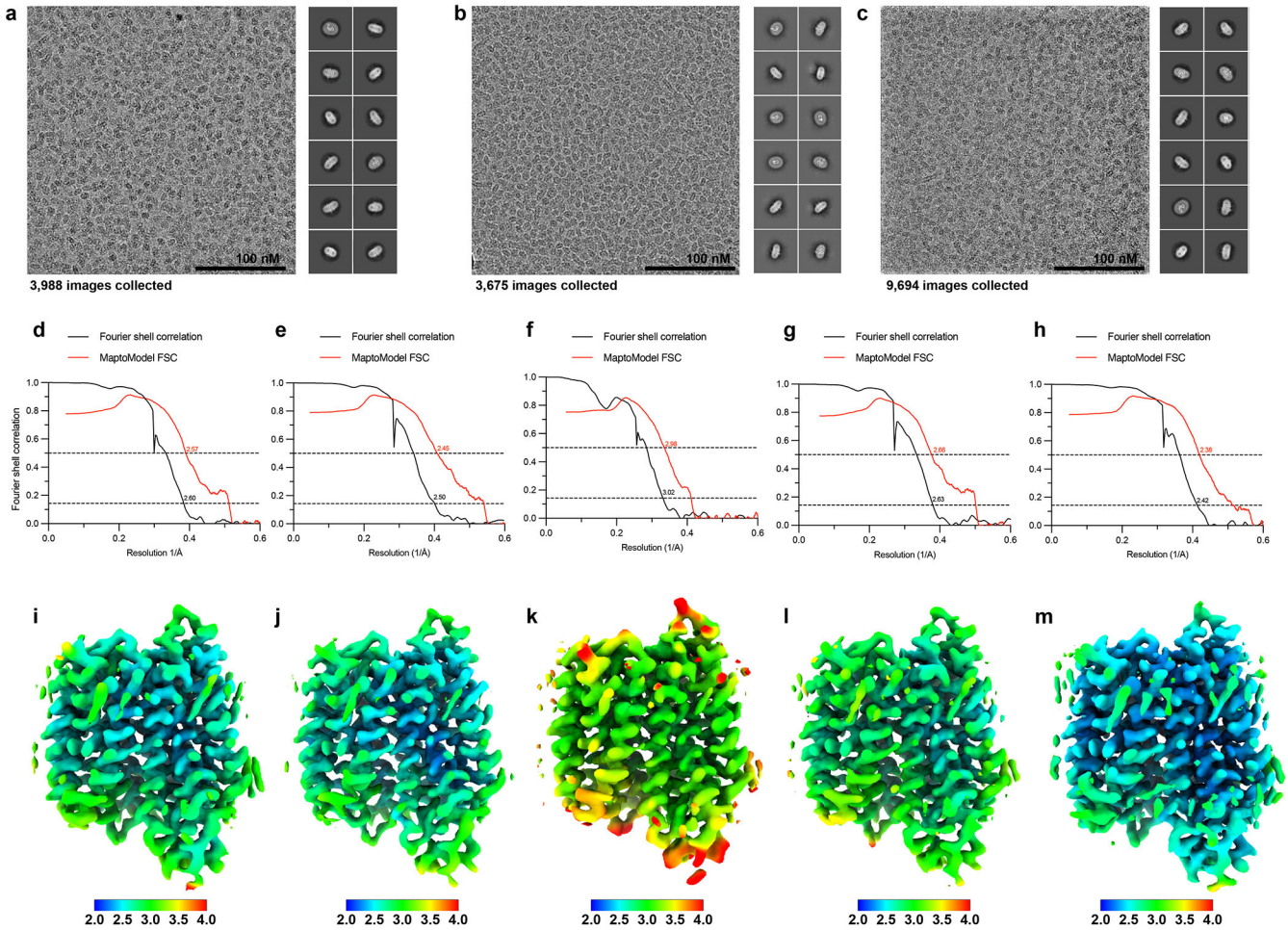

Extended Data Fig. 2: Validation of cryo-EM structures of FLVCR1.

a-c Representative cryo-EM images and two-dimensional class averages of human FLVCR1 in 1 mM choline (a), 1 mM ethanolamine (b) or without added substrate (c). Number of collected cryo-EM images are shown. **d-h,** Plots showing Fourier shell correlations between two independent half-maps (black) and between density-modified map and refined atomic model (red) for choline-bound FLVCR1 (d), ethanolamine-bound FLVCR1 (e), endogenous choline-bound FLVCR1 obtained from FLVCR1 incubated with 1mM ethanolamine (f), endogenous choline-bound FLVCR1 obtained from FLVCR1 without exogenous ligand incubation (g), and endogenous ligand-bound FLVCR1 obtained from FLVCR1 without exogenous ligand incubation (h). Dashed lines are indicated at FSC = 0.5 and FSC = 0.143. **i-m,** Local resolution plots of choline-bound FLVCR1 (i), ethanolamine-bound FLVCR1 (j), endogenous-choline bound FLVCR1 obtained from FLVCR1 incubated with 1mM ethanolamine (k), endogenous choline-bound FLVCR1 obtained from FLVCR1 without exogenous substrate incubation (l), and endogenous ligand-bound FLVCR1 obtained from FLVCR1 without exogenous ligand incubation (m).

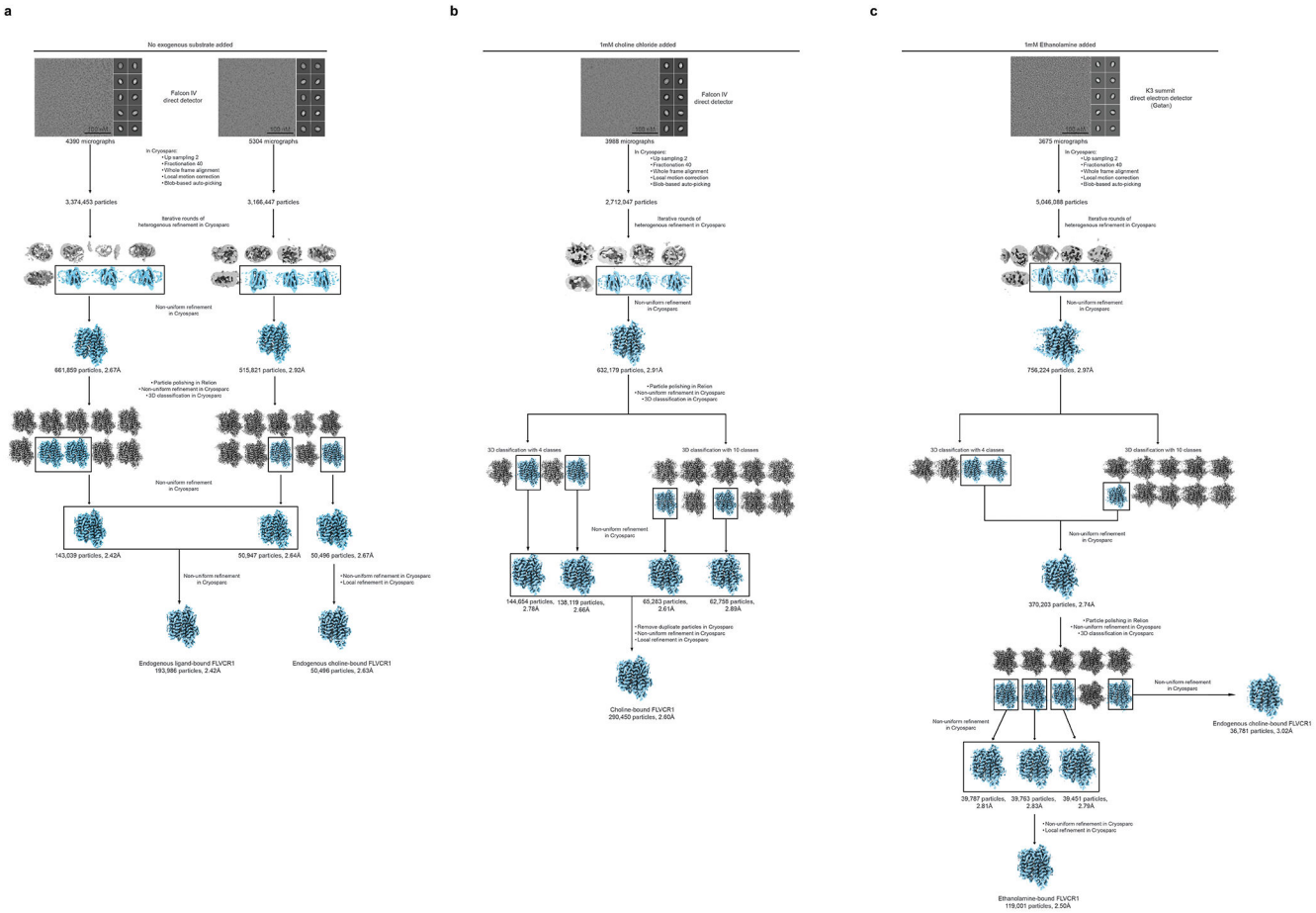

Extended Data Fig. 3: Cryo-EM analysis of hFLVCR1.

Flow-chart summarizing Cryo-EM image acquisition and processing of human FLVCR1 without added substrate (a), in 1 mM choline (b), or 1 mM ethanolamine (c). Number of collected cryo-EM images and selected particles are shown.

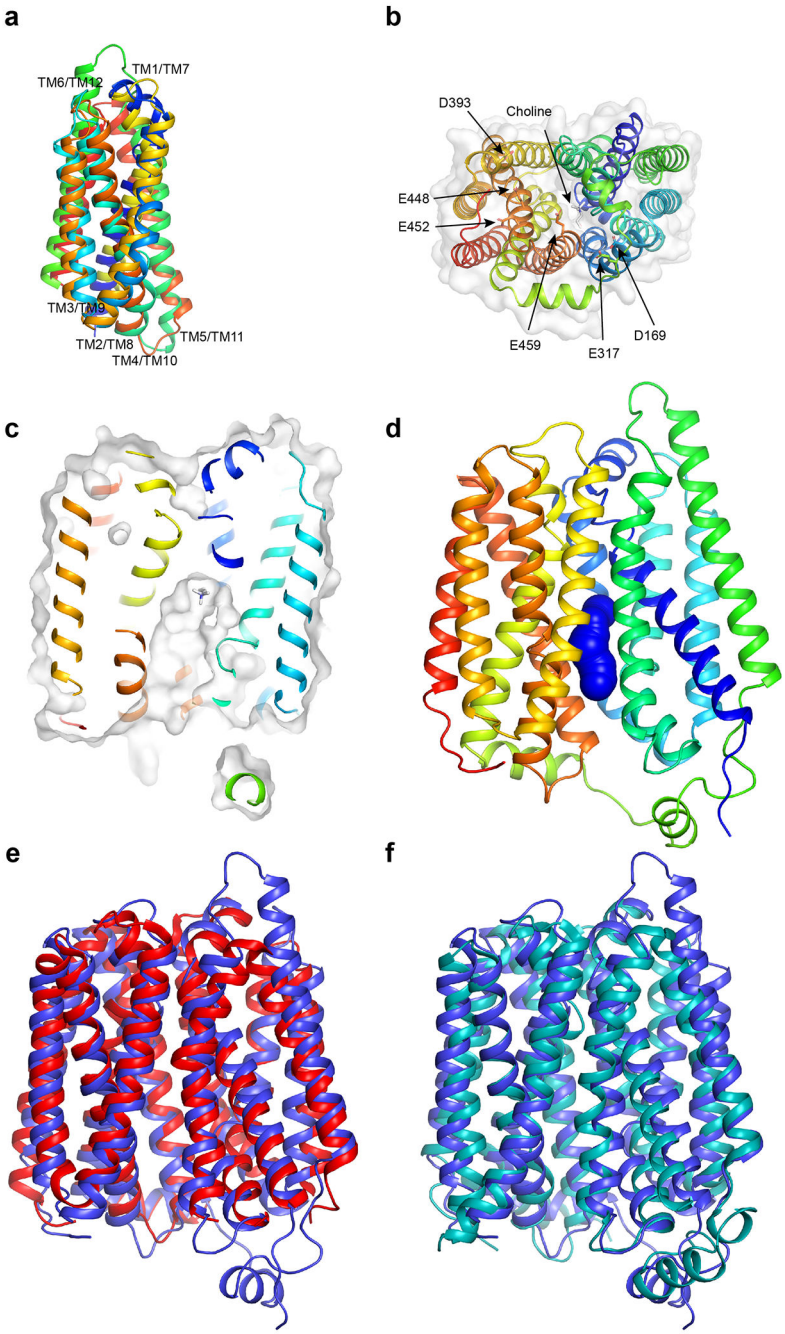

Extended Data Fig. 4: Choline-bound FLVCR1 adopts an inward-facing conformation.

a, Superposition of TM1-6 and TM7-12. RMSD = 3.5 Å. **b,** Central cavity viewed from the cytosolic side. Aspartate and glutamate residues in and near the entrance to the central cavity are shown as sticks. **c,** Central section of choline-bound FLVCR1 is contiguous with choline shown as sticks. **d,** Blue spheres depict the minimum radius of the central cavity in the choline-bound state as a function of position. **e-f,** Superposition of choline-bound FLVCR1 (blue) with *E. coli* SotB (D; PDB: 6KKL; RMSD = 2.3 Å; red) (e) or *E. coli* DgoT (E; PDB: 6E9N; RMSD = 2.6 Å; cyan) (f).

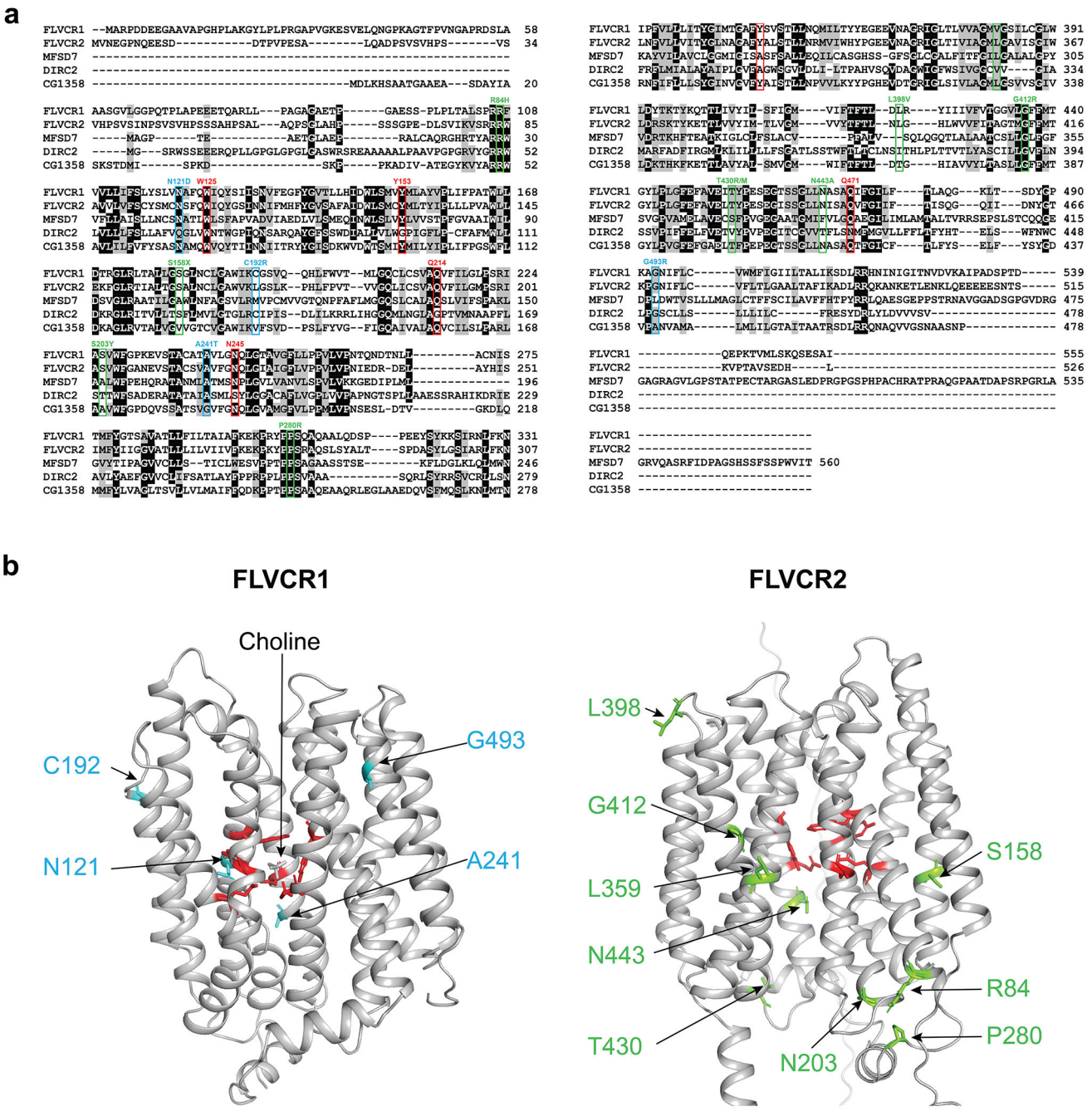

Extended Data Fig. 5: Sequence alignment of SLC49A family members and identified disease-associated mutations.

a, Sequence alignment of human FLVCR1 (SLC49A1), human FLVCR2 (SLC49A2), human MFSD7 (SLC49A3), human DIRC2 (SLC49A4) and *Drosophila* CG1358 performed using Clustal Omega [55] and pyBoxshade (https://github.com/mdbaron42/pyBoxshade). Substrate-binding site residues are highlighted by red boxes. Residues whose mutation leads to PCARP or Fowler syndrome are highlighted by blue and green boxes, respectively. **b,** Structure of choline-bound FLVCR1 (left) and Alphafold2 model of FLVCR2 (right) [56] with

residues whose mutation leads to PCARP and Fowler syndrome highlighted in blue and green, respectively. FLVCR1 substrate binding site residues and the corresponding residues in FLVCR2 are highlighted in red.

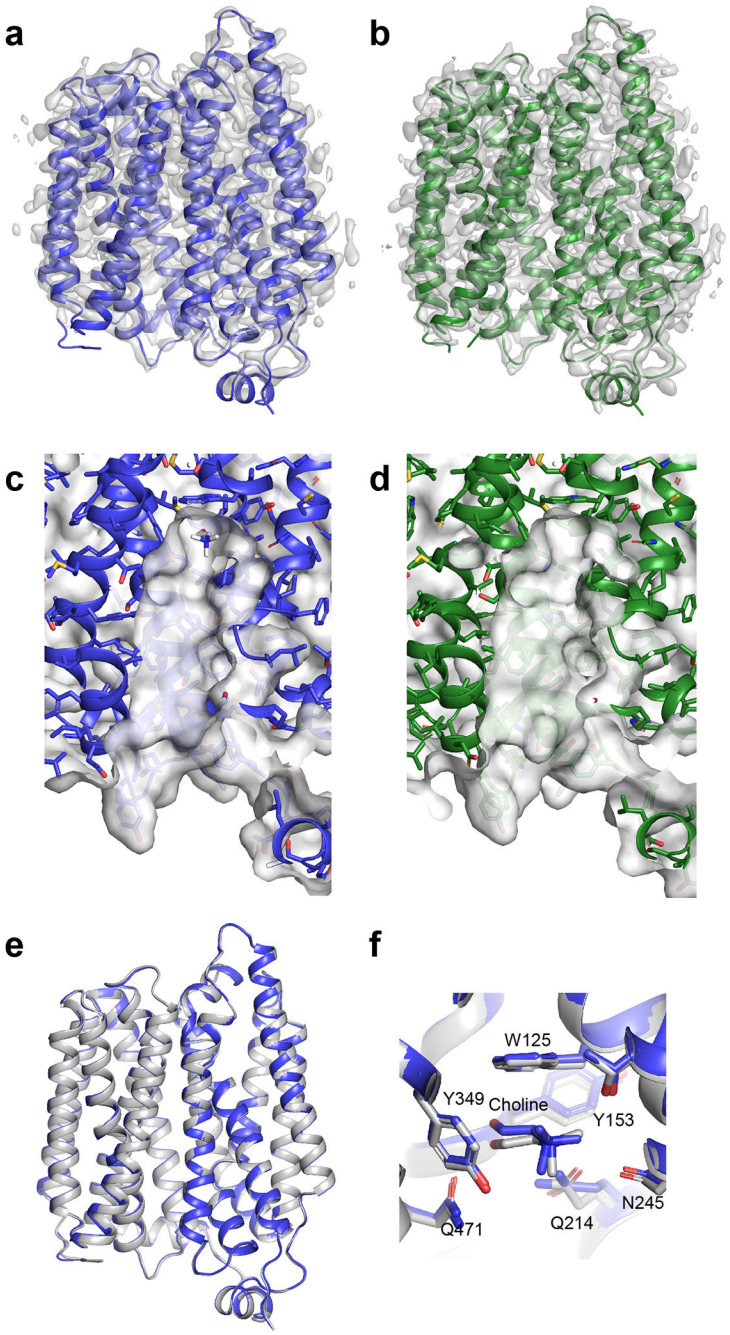

Extended Data Fig. 6: Cryo-EM structures of FLVCR1 determined in a substrate-free condition.
a-b, Cryo-EM density maps and atomic models of FLVCR1 in endogenous choline (a) and endogenous ligand-bound (b) states. **c-d,** Central slice of the central cavity of choline-bound (c) and endogenous ligand-bound (d) states, with surface colored white. Choline is

shown as sticks in c. Endogenous ligand is not modeled or shown in d. **e,** Superposition of choline-bound (grey) and endogenous choline-bound (blue) states. **f,** Superposition of substrate-binding sites in choline-bound (grey) and endogenous choline-bound (blue) states.

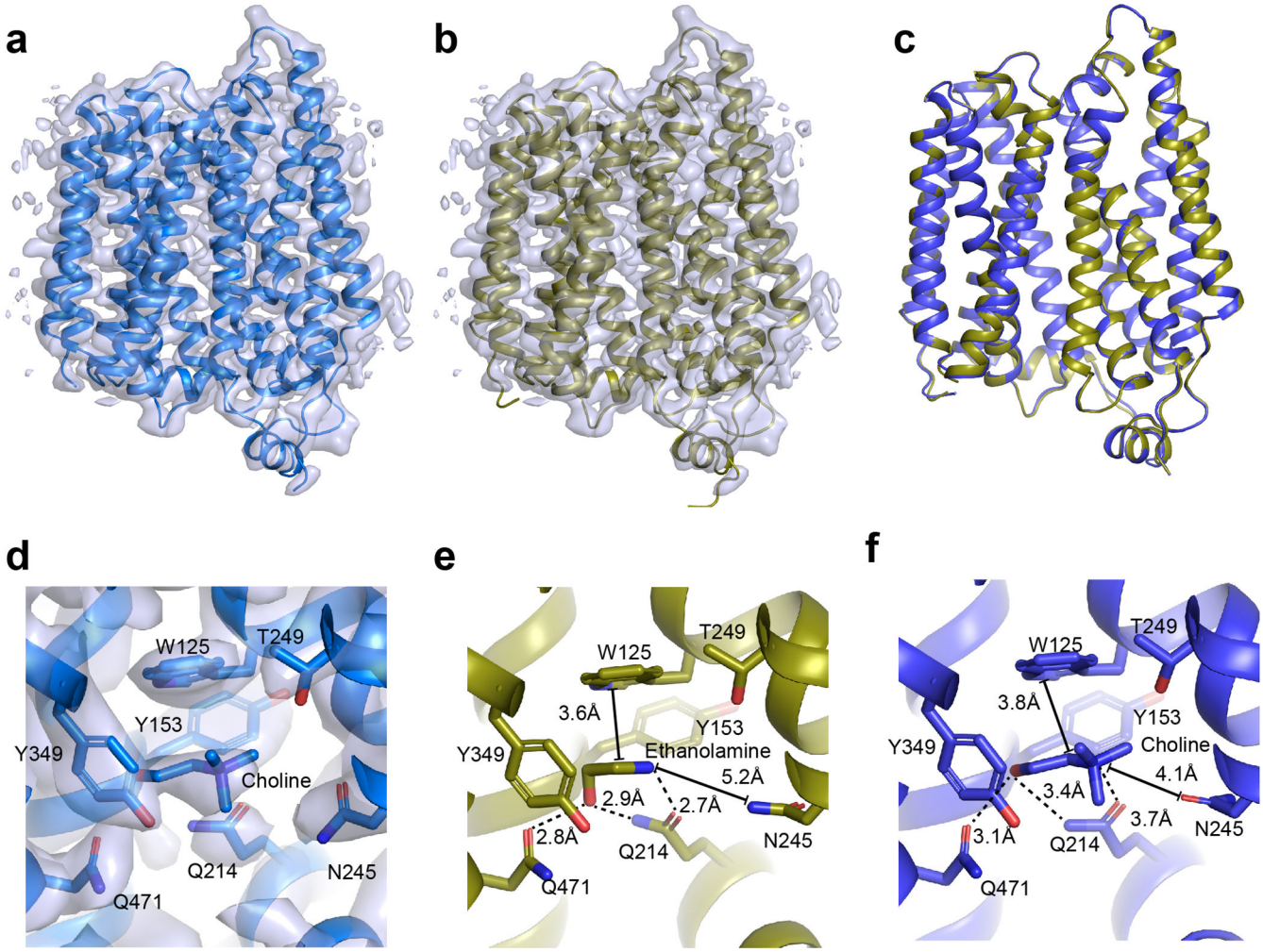

Extended Data Fig. 7: Cryo-EM structures of FLVCR1 determined in 1 mM ethanolamine.

a-b Cryo-EM density maps of endogenous choline-bound FLVCR1 (a) and ethanolamine-bound FLVCR1 (b) states, determined from particles imaged in the presence of 1 mM ethanolamine. **c,** Superposition of ethanolamine-bound (gold) and choline-bound (blue) states. **d,** Substrate-binding site in endogenous choline-bound FLVCR1 state, determined from particles imaged in the presence of 1 mM ethanolamine. Residues and modelled substrates are shown as sticks. Density is shown as a grey isosurface and contoured at 3.0 σ. **e-f,** Coordination of ethanolamine in the substrate-binding site in ethanolamine-bound state (e) and choline in the substrate-binding site in the choline-bound state (f). Polar interactions are shown as dashed lines and distances as solid lines.

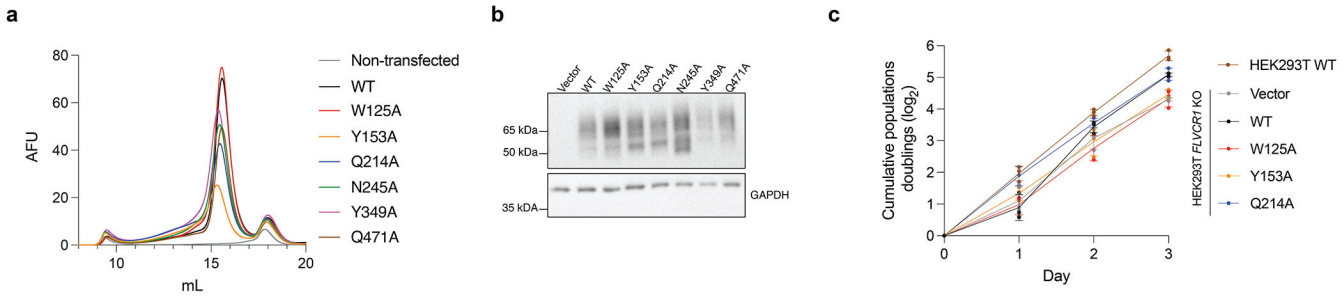

Extended Data Fig. 8: FLVCR1 substrate-binding site mutants.

a, FSEC analysis of wild-type or substrate-binding site mutants fused to mCerulean expressed in *FLVCR1*-knockout HEK293T cells. **b,** Western blot analysis of *FLVCR1*-knockout HEK293T cells expressing a vector control or wild-type or mutant *FLVCR1* cDNA. GAPDH was ran on a separate gel as sample processing controls. For western blot source data, see Supplementary Fig.1. **c**, Cumulative $\log_2$ fold change in cell number of HEK293T cells and *FLVCR1*-knockout HEK293T cells expressing a vector control or wild-type or mutant *FLVCR1* cDNA. n=3 biologically independent samples. (P-values: HEK293T WT and HEK293T *FLVCR1* KO + *FLVCR1* WT cDNA; $p=3x10^{-3}$, HEK293T *FLVCR1* KO + *FLVCR1* WT cDNA and HEK293T *FLVCR1* KO + *FLVCR1* Q214A cDNA; $p=9x10^{-1}$, HEK293T *FLVCR1* KO + Vector and HEK293T *FLVCR1* KO + *FLVCR1* W125A cDNA; $p=9x10^{-1}$, HEK293T *FLVCR1* KO + Vector and HEK293T *FLVCR1* KO + *FLVCR1* Y153A cDNA; $p=1x10^{-1}$, HEK293T *FLVCR1* KO + *FLVCR1* WT cDNA and HEK293T *FLVCR1* KO + Vector; $p=8x10^{-5}$.)

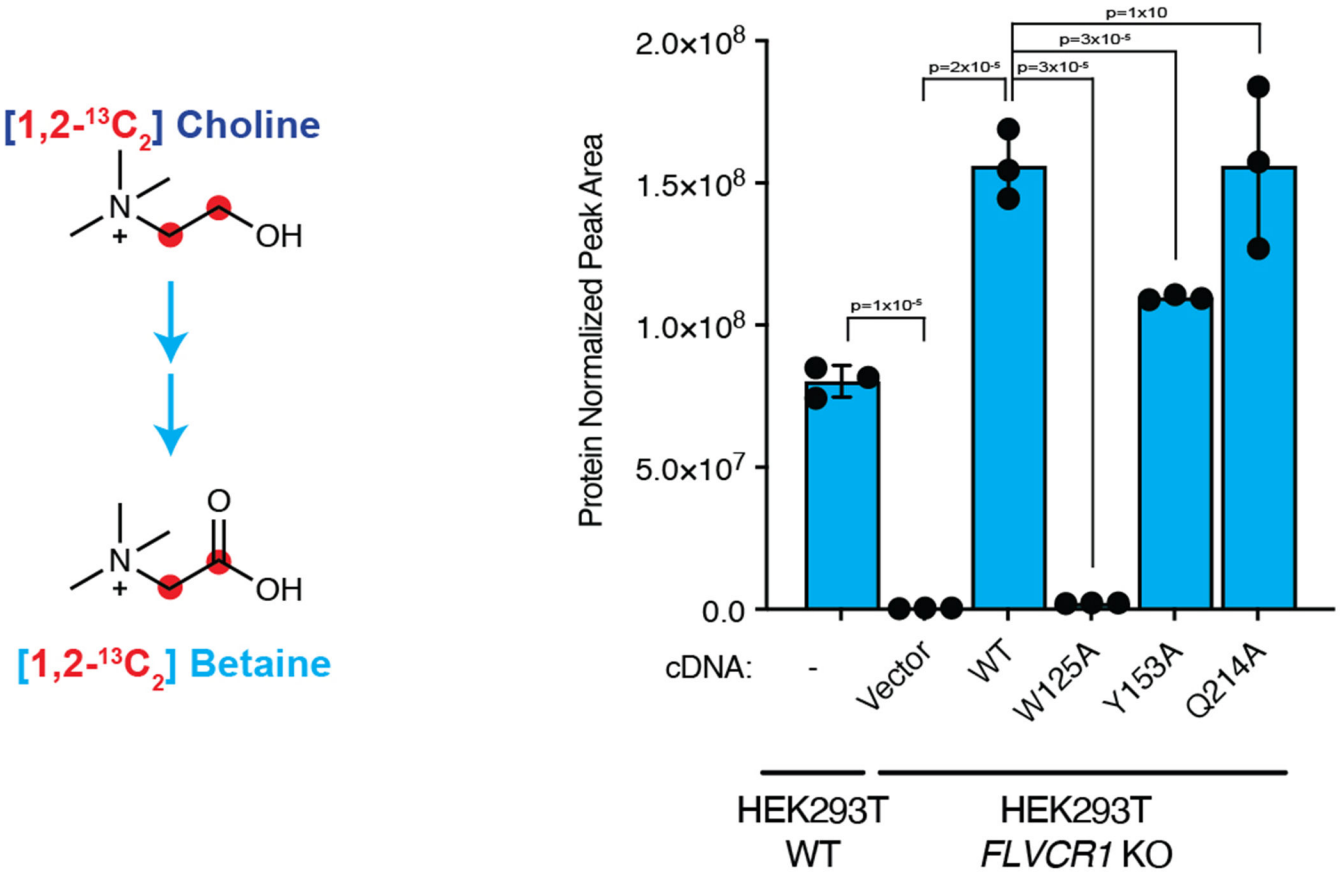

Extended Data Fig. 9: Incorporation of labeled choline into betaine requires FLVCR1.

Schematic for tracing [1,2-$^{13}C_2$] choline into betaine (left) and the abundance of betaine M+2 after incubation with 21.5 μM [1,2-$^{13}C_2$] choline for 1 hour in *FLVCR1*-knockout HEK293T cells expressing a vector control or wild-type or mutant *FLVCR1* cDNA (right). n=3 biologically independent samples.

Extended Data Table 1:

Cryo-EM data collection, refinement, and validation statistics.

	#1 Choline-bound hFLVCR (EMD-42107) (PDB 8UBW)	#2 Endogenous choline-bound hFLVCR1 (no exogenous substrate) (EMD-42109) (PDB 8UBY)	#3 Endogenous ligand-bound hFLVCR1 (EMD-42111) (PDB 8UC0)	#4 Ethanolamine-bound hFLVCR1 (EMD-42108) (PDB 8UBX)	#5 Endogenous choline-bound hFLVCR1 (1 mM ethanolamine) (EMD-42110) (8UBZ)
Data collection and processing					
Magnification	165000X	165000X	165000X	29,000X	29,000X
Voltage (kV)	300	300	300	300	300
Electron exposure (e–/Å^2)	53.98	53.98	53.98	66	66

	#1 Choline-bound hFLVCR (EMD-42107) (PDB 8UBW)	**#2 Endogenous choline-bound hFLVCR1 (no exogenous substrate) (EMD-42109) (PDB 8UBY)**	**#3 Endogenous ligand-bound hFLVCR1 (EMD-42111) (PDB 8UC0)**	**#4 Ethanolamine-bound hFLVCR1 (EMD-42108) (PDB 8UBX)**	**#5 Endogenous choline-bound hFLVCR1 (1 mM ethanolamine) (EMD-42110) (8UBZ)**
Defocus range (μm)	−0.5 to −1.5	−0.5 to −1.5	−0.5 to −1.5	−0.5 to −1.5	−0.5 to −1.5
Pixel size (Å)	0.725	0.725	0.725	0.826	0.826
Symmetry imposed	C1	C1	C1	C1	C1
Initial particle images (no.)	2,712,047	6,540,900	6,540,900	5,046,088	5,046,088
Final particle images (no.)	290,450	50,496	193,986	119,001	36,781
Map resolution (Å)	2.60	2.63	2.42	2.50	3.02
FSC threshold	0.143	0.143	0.143	0.143	0.143
Map resolution range (Å)	2.30-4.05	2.37-23.41	2.13-6.94	2.23-3.6	2.75-11.68
Refinement					
Initial model used (PDB code)	Initial model generated by ModelAngelo	8UBW	Initial model generated by ModelAngelo	8UBW	8UBW
Model resolution (Å)	2.57	2.66	2.38	2.45	2.98
FSC threshold	0.5	0.5	0.5	0.5	0.5
Map sharpening *B* factor (Å^2)	−30	−30	−30	−30	−30
Model composition					
Non-hydrogen atoms	3398	3411	3486	3429	3359
Protein residues	418	419	422	419	415
Ligands	4	4	4	4	4
B factors (Å^2)					
Protein	51.43	51.97	40.75	45.16	60.56
Ligand	60.83	61.77	56.95	58.91	71.97
R.m.s. deviations					
Bond lengths (Å)	0.002	0.002	0.002	0.002	0.002
Bond angles (°)	0.475	0.473	0.473	0.506	0.481
Validation					
MolProbity score	1.15	1.17	1.26	1.19	1.22
Clashscore	3.64	3.78	4.92	4.08	4.41
Poor rotamers (%)	0.85	0.56	0.84	0.56	0.28
Ramachandran plot					
Favored (%)	98.56	98.32	98.81	98.08	98.55
Allowed (%)	1.14	1.68	1.19	1.92	1.45
Disallowed (%)	0	0	0	0	0

Acknowledgements

We thank M. J. de la Cruz and the SEMC staff for help with data acquisition; the Memorial Sloan Kettering Cancer Center HPC group for assistance with data processing and the members of the laboratories for comments on the manuscript and L. Finley for helpful discussions. R.H. is supported by the NIH-National Cancer Institute Cancer Center Support Grant P30-CA008748 and is a Searle Scholar. T.K. is supported by NIH/NIDDK (F32 DK127836), the Shapiro-Silverberg Fund for the Advancement of Translational Research and a Merck Postdoctoral Fellowship at The Rockefeller University. K.B. is supported by the NIH/NIDDK (R01 DK123323-01), Mark Foundation Emerging Leader Award; and is a Searle and Pew-Stewart Scholar. Some of this work was performed at the Simons Electron Microscopy Center at the New York Structural Biology Center, with major support from the Simons Foundation (SF349247).

Data availability

Cryo-EM maps have been deposited in the EMDB under accession codes EMD-42107 [https://www.ebi.ac.uk/emdb/EMD-42107] (choline-bound FLVCR1), EMD-42108 [https://www.ebi.ac.uk/emdb/EMD-42108] (ethanolamine-bound FLVCR1), EMD-42109 [https://www.ebi.ac.uk/emdb/EMD-42109] (endogenous choline-bound FLVCR1), EMD-42110 [https://www.ebi.ac.uk/emdb/EMD-42110] (endogenous choline-bound FLVCR1, from images collected in 1 mM ethanolamine) and [https://www.ebi.ac.uk/emdb/EMD-42111] EMD-42111 (endogenous ligand-bound FLVCR1). Atomic coordinates have been deposited in the PDB under accession codes 8UBW [https://doi.org/10.2210/pdb8UBW/pdb] (choline-bound FLVCR1), 8UBX [https://doi.org/10.2210/pdb8UBX/pdb] (ethanolamine-bound FLVCR1), 8UBY [https://doi.org/10.2210/pdb8UBY/pdb] (endogenous choline-bound FLVCR1), 8UBZ [https://doi.org/10.2210/pdb8UBZ/pdb] (endogenous choline-bound FLVCR1, from images collected in 1 mM ethanolamine) and 8UC0 [https://doi.org/10.2210/pdb8UC0/pdb] (endogenous ligand-bound FLVCR1). The atomic coordinates of previously published structures of *E. coli* SotB [https://doi.org/10.2210/6KKL/pdb] in an inward-facing state and *E. coli* DgoT [https://doi.org/10.2210/6E9N/pdb] in an inward-facing state were used in this study. Co-dependencies between *FLVCR1* and all genes computed from CRISPR DepMap Chronos 2023Q2 used in this study were downloaded from https://depmap.org/portal/all. Source data is available with this paper.

References

1. Vance JE Phospholipid Synthesis and Transport in Mammalian Cells. Traffic 16, 1–18 (2015). [PubMed: 25243850]
2. Patel D & Witt SN Ethanolamine and Phosphatidylethanolamine: Partners in Health and Disease. Oxid. Med. Cell. Longev 2017, 4829180 (2017). [PubMed: 28785375]
3. Kent C Phospholipid Metabolism in Mammals. Encycl. Biol. Chem 3, 314–320 (2004).
4. Kennedy EP Sailing to Byzantium. Annu. Rev. Biochem 61, 1–28 (1992). [PubMed: 1497305]
5. Gibellini F & Smith TK The Kennedy pathway--De novo synthesis of phosphatidylethanolamine and phosphatidylcholine. IUBMB Life 62, 414–428 (2010). [PubMed: 20503434]
6. Kennedy EP SYNTHESIS OF PHOSPHATIDES IN ISOLATED MITOCHONDRIA: II. INCORPORATION OF CHOLINE INTO LECITHIN. J. Biol. Chem 209, 525–535 (1954). [PubMed: 13192105]
7. Yanatori I, Yasui Y, Miura K & Kishi F Mutations of FLVCR1 in posterior column ataxia and retinitis pigmentosa result in the loss of heme export activity. Blood Cells, Mol. Dis 49, 60–66 (2012). [PubMed: 22483575]
8. Rajadhyaksha AM et al. Mutations in FLVCR1 cause posterior column ataxia and retinitis pigmentosa. Am. J. Hum. Genet 87, 643–654 (2010). [PubMed: 21070897]

9. Khan AA & Quigley JG Heme and FLVCR-related transporter families SLC48 and SLC49. Mol. Aspects Med 34, 669–682 (2013). [PubMed: 23506900]
10. Corbin KD & Zeisel SH Choline metabolism provides novel insights into nonalcoholic fatty liver disease and its progression. Curr. Opin. Gastroenterol 28, 159–165 (2012). [PubMed: 22134222]
11. Kenny TC et al. Integrative genetic analysis identifies FLVCR1 as a plasma-membrane choline transporter in mammals. Cell Metab. (2023) doi:10.1016/j.cmet.2023.04.003.
12. Tsuchiya M, Tachibana N, Nagao K, Tamura T & Hamachi I Organelle-selective click labeling coupled with flow cytometry allows pooled CRISPR screening of genes involved in phosphatidylcholine metabolism. Cell Metab. 35, 1072–1083.e9 (2023). [PubMed: 36917984]
13. Kvarnung M et al. Mutations in FLVCR2 associated with Fowler syndrome and survival beyond infancy. Clin. Genet 89, 99–103 (2016). [PubMed: 25677735]
14. Meyer E et al. Mutations in FLVCR2 are associated with proliferative vasculopathy and hydranencephaly-hydrocephaly syndrome (Fowler syndrome). Am. J. Hum. Genet 86, 471–478 (2010). [PubMed: 20206334]
15. Lalonde E et al. Unexpected allelic heterogeneity and spectrum of mutations in Fowler syndrome revealed by next-generation exome sequencing. Hum. Mutat 31, 918–923 (2010). [PubMed: 20518025]
16. Drew D, North RA, Nagarathinam K & Tanabe M Structures and General Transport Mechanisms by the Major Facilitator Superfamily (MFS). Chem. Rev 121, 5289–5335 (2021). [PubMed: 33886296]
17. Sauve S, Williamson J, Polasa A & Moradi M Ins and Outs of Rocker Switch Mechanism in Major Facilitator Superfamily of Transporters. Membranes (Basel). 13, (2023).
18. Yan N Structural Biology of the Major Facilitator Superfamily Transporters. Annu. Rev. Biophys 44, 257–283 (2015). [PubMed: 26098515]
19. Zhang XC, Zhao Y, Heng J & Jiang D Energy coupling mechanisms of MFS transporters. Protein Sci. 24, 1560–1579 (2015). [PubMed: 26234418]
20. Okuda T et al. Identification and characterization of the high-affinity choline transporter. Nat. Neurosci 3, 120–125 (2000). [PubMed: 10649566]
21. Ferguson SM et al. Lethal impairment of cholinergic neurotransmission in hemicholinium-3-sensitive choline transporter knockout mice. Proc. Natl. Acad. Sci 101, 8762–8767 (2004). [PubMed: 15173594]
22. Iwamoto H, Blakely RD & De Felice LJ Na+, Cl-, and pH dependence of the human choline transporter (hCHT) in Xenopus oocytes: the proton inactivation hypothesis of hCHT in synaptic vesicles. J. Neurosci. Off. J. Soc. Neurosci 26, 9851–9859 (2006).
23. Mödinger Y, Schön C, Wilhelm M & Hals P-A Plasma Kinetics of Choline and Choline Metabolites After A Single Dose of SuperbaBoostTM Krill Oil or Choline Bitartrate in Healthy Volunteers. Nutrients vol. 11 (2019).
24. Garguilo MG & Michael AC Amperometric microsensors for monitoring choline in the extracellular fluid of brain. J. Neurosci. Methods 70, 73–82 (1996). [PubMed: 8982984]
25. Brehm R, Lindmar R & Löffelholz K Muscarinic mobilization of choline in rat brain in vivo as shown by the cerebral arterio-venous difference of choline. J. Neurochem 48, 1480–1485 (1987). [PubMed: 3559562]
26. Bianchi L et al. Extracellular levels of amino acids and choline in human high grade gliomas: an intraoperative microdialysis study. Neurochem. Res 29, 325–334 (2004). [PubMed: 14992293]
27. Plagemann PG Choline metabolism and membrane formation in rat hepatoma cells grown in suspension culture. 3. Choline transport and uptake by simple diffusion and lack of direct exchange with phosphatidylcholine. J. Lipid Res 12, 715–724 (1971). [PubMed: 4330925]
28. Oswald C et al. Crystal structures of the choline/acetylcholine substrate-binding protein ChoX from Sinorhizobium meliloti in the liganded and unliganded-closed states. J. Biol. Chem 283, 32848–32859 (2008). [PubMed: 18779321]
29. Bärland N et al. Mechanistic basis of choline import involved in teichoic acids and lipopolysaccharide modification. Sci. Adv 8, (2022).
30. Holm L Dali server: structural unification of protein families. Nucleic Acids Res. 50, W210–W215 (2022). [PubMed: 35610055]

31. Xiao Q et al. Visualizing the nonlinear changes of a drug-proton antiporter from inward-open to occluded state. Biochem. Biophys. Res. Commun 534, 272–278 (2021). [PubMed: 33280821]
32. Leano JB et al. Structures suggest a mechanism for energy coupling by a family of organic anion transporters. PLoS Biol. 17, e3000260 (2019). [PubMed: 31083648]
33. Quigley JG et al. Identification of a human heme exporter that is essential for erythropoiesis. Cell 118, 757–766 (2004). [PubMed: 15369674]
34. Tsherniak A et al. Defining a Cancer Dependency Map. Cell 170, 564–576.e16 (2017). [PubMed: 28753430]
35. Wainberg M et al. A genome-wide atlas of co-essential modules assigns function to uncharacterized genes. Nat. Genet 53, 638–649 (2021). [PubMed: 33859415]
36. Jackson BT Identification of metabolic networks by genetic co-essentiality analysis. Nat. Rev. Mol. Cell Biol 24, 378 (2023). [PubMed: 37101011]
37. Lykidis A, Wang J, Karim MA & Jackowski S Overexpression of a mammalian ethanolamine-specific kinase accelerates the CDP-ethanolamine pathway. J. Biol. Chem 276, 2174–2179 (2001). [PubMed: 11044454]
38. Vermeulen PS, Geelen MJH & van Golde LMG Substrate specificity of CTP : Phosphoethanolamine cytidylyltransferase purified from rat liver. Biochim. Biophys. Acta - Lipids Lipid Metab 1211, 343–349 (1994).
39. Kenny TC et al. Integrative genetic analysis identifies FLVCR1 as a plasma-membrane choline transporter in mammals. Cell Metab. 35, 1057–1071.e12 (2023). [PubMed: 37100056]
40. Taylor A, Grapentine S, Ichhpuniani J & Bakovic M Choline transporter-like proteins 1 and 2 are newly identified plasma membrane and mitochondrial ethanolamine transporters. J. Biol. Chem 296, 100604 (2021). [PubMed: 33789160]
41. Navale AM & Paranjape AN Glucose transporters: physiological and pathological roles. Biophys. Rev. 8, 5–9 (2016).
42. Goehring A et al. Screening and large-scale expression of membrane proteins in mammalian cells for structural studies. Nat. Protoc. 9, 2574–2585 (2014). [PubMed: 25299155]
43. Mastronarde DN Automated electron microscope tomography using robust prediction of specimen movements. J. Struct. Biol. 152, 36–51 (2005). [PubMed: 16182563]
44. Suloway C et al. Fully automated, sequential tilt-series acquisition with Leginon. J. Struct. Biol. 167, 11–18 (2009). [PubMed: 19361558]
45. Punjani A, Rubinstein JL, Fleet DJ & Brubaker MA cryoSPARC: algorithms for rapid unsupervised cryo-EM structure determination. Nat. Methods 14, 290–296 (2017). [PubMed: 28165473]
46. Punjani A, Zhang H & Fleet DJ Non-uniform refinement: adaptive regularization improves single-particle cryo-EM reconstruction. Nat. Methods 17, 1214–1221 (2020). [PubMed: 33257830]
47. Scheres SHW Chapter Six – Processing of Structurally Heterogeneous Cryo-EM Data in RELION. In The Resolution Revolution: Recent Advances In cryoEM (ed. Crowther R. A. B. T.-M. in E.) vol. 579 125–157 (Academic Press, 2016).
48. Terwilliger TC, Ludtke SJ, Read RJ, Adams PD & Afonine PV Improvement of cryo-EM maps by density modification. Nat. Methods 17, 923–927 (2020). [PubMed: 32807957]
49. Jamali K, Kimanius D & Scheres SHW. A Graph Neural Network Approach to Automated Model Building in Cryo-EM Maps. in (2022).
50. Emsley P, Lohkamp B, Scott WG & Cowtan K Features and development of {\it Coot}. Acta Crystallogr. Sect. D 66, 486–501 (2010). [PubMed: 20383002]
51. Adams PD et al. {\it PHENIX}: a comprehensive Python-based system for macromolecular structure solution. Acta Crystallogr. Sect. D 66, 213–221 (2010). [PubMed: 20124702]
52. Pettersen EF et al. UCSF Chimera—A visualization system for exploratory research and analysis. J. Comput. Chem. 25, 1605–1612 (2004). [PubMed: 15264254]
53. Pettersen EF et al. UCSF ChimeraX: Structure visualization for researchers, educators, and developers. Protein Sci. 30, 70–82 (2021). [PubMed: 32881101]
54. Pavelka A et al. CAVER: Algorithms for Analyzing Dynamics of Tunnels in Macromolecules. IEEE/ACM Trans. Comput. Biol. Bioinforma. 13, 505–517 (2016).

55. Sievers F et al. Fast, scalable generation of high-quality protein multiple sequence alignments using Clustal Omega. Mol. Syst. Biol. 7, 539 (2011). [PubMed: 21988835]

56. Jumper J et al. Highly accurate protein structure prediction with AlphaFold. Nature 596, 583–589 (2021). [PubMed: 34265844]

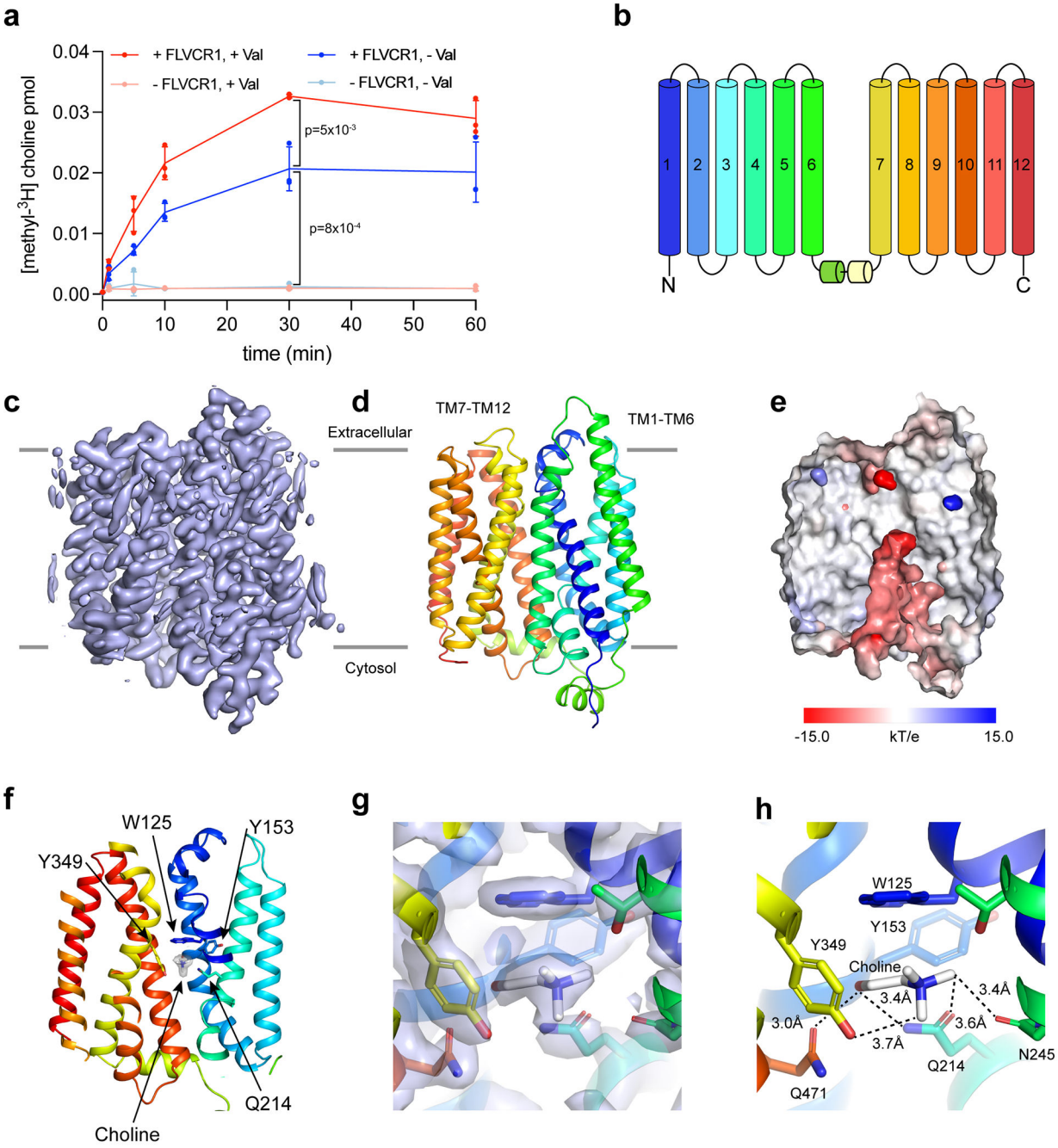

Fig. 1: Structure of human FLVCR1 in a choline-bound state.

a, Uptake of 20 nM [methyl-^{3}H]choline by liposomes containing FLVCR1 in the presence (red) or absence (blue) of 1 μM valinomycin or by protein-free liposomes in the presence (pink) or absence (light-blue) of 1 μM valinomycin. n=3 technically independent samples. **b,** Schematic of FLVCR1 colored by helix. **c-d,** Cryo-EM density map (c) and model of FLVCR1 (d). Model is colored by helix as in b. Grey lines correspond to the approximate position of the membrane. **e,** Central slice of FLVCR1 with surface colored by electrostatic potential. **f,** Central slice of FLVCR1 with choline and choline-coordinating residues shown

as sticks. Density is shown as a grey isosurface and contoured at 3.0 σ. **g-h,** Choline-binding site. Residues that comprise the substrate-binding site are shown as sticks. Density is shown as a grey isosurface in (g) and contoured at 3.0 σ.

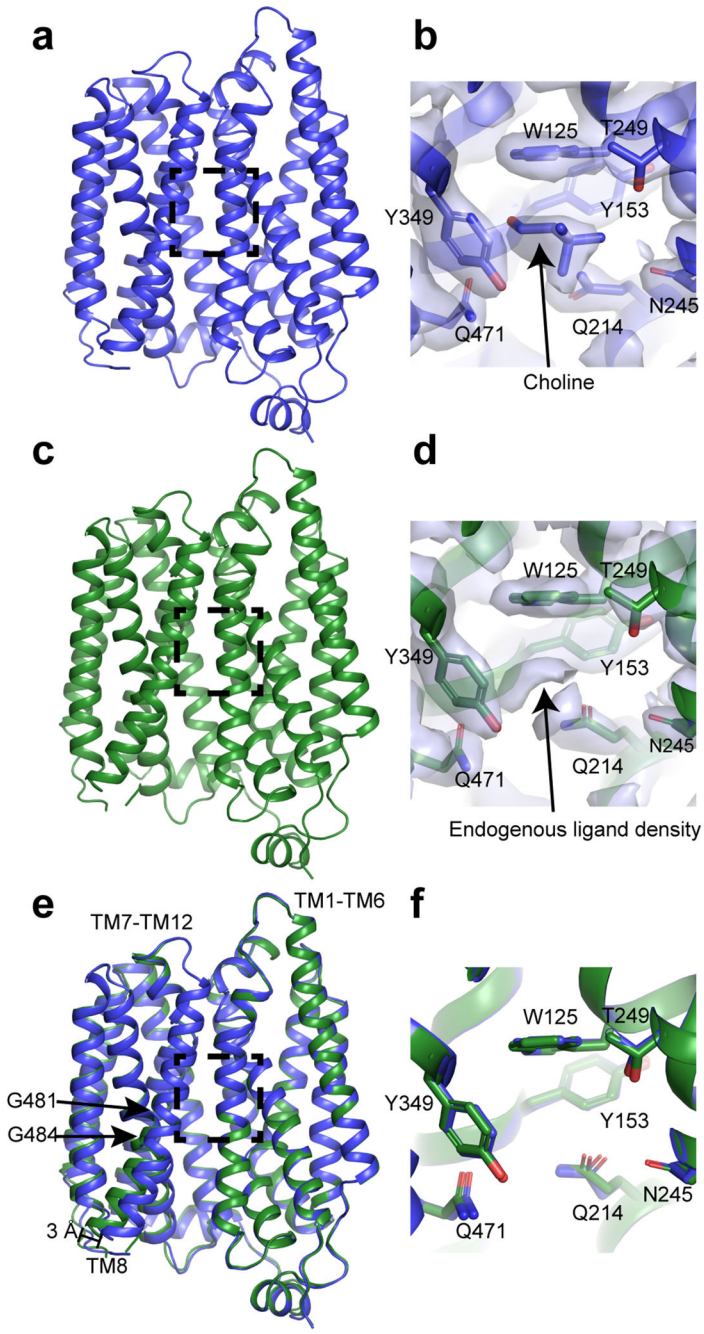

Fig. 2: FLVCR1 bound to endogenous substrates.

a,c, FLVCR1 in endogenous choline-bound (a) or endogenous ligand-bound (c) states, determined from particles imaged in the absence of exogenous substrate. Dashed box corresponds to the substrate-binding sites shown in b and d. **b,d,** Substrate-binding sites in endogenous choline-bound (b) or endogenous ligand-bound (d) states, determined from particles imaged in the absence of exogenous substrate. Residues and modelled substrates are shown as sticks. Density is shown as a grey isosurface and contoured at 3.0 σ. **e,** Superposition of endogenous choline-bound (blue) and endogenous ligand-bound (green)

states. **f,** Superposition of substrate-binding sites in endogenous choline-bound (blue) and endogenous ligand-bound (green). Substrates are not depicted.

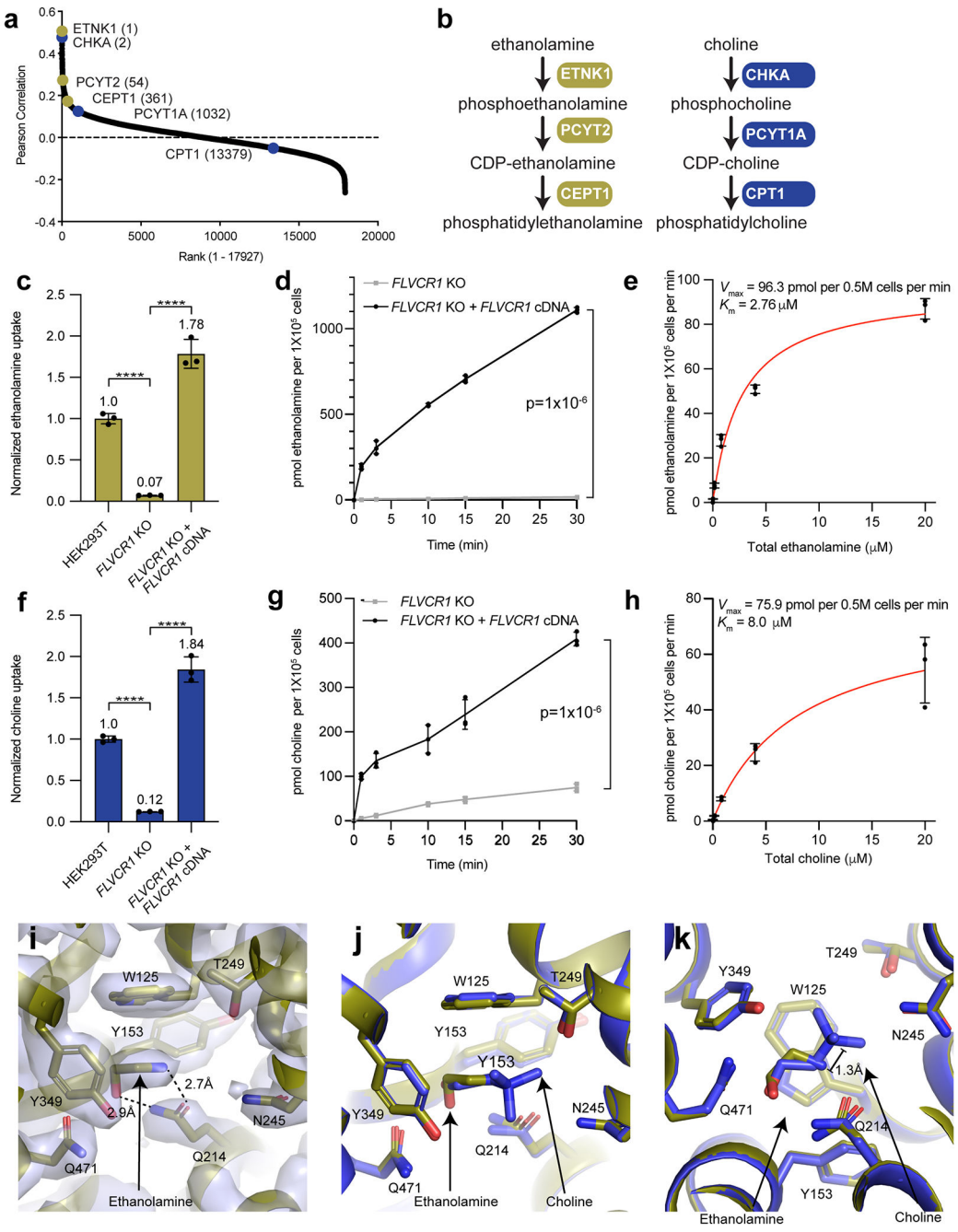

Fig. 3: Ethanolamine and choline are transported by FLVCR1 through a common pathway.

a, Pearson correlation of co-dependencies between *FLVCR1* and all genes computed from CRISPR DepMap Chronos 2023Q2. Genes in the ethanolamine (gold) and choline (blue) branches of the Kennedy pathway are highlighted. **b,** Schematic of the ethanolamine (left) and choline (right) branches of the Kennedy pathway. **c,f,** Uptake of 2 μM ethanolamine (1.86 nM ethanolamine [1-^{3}H] hydrochloride) (c) or 21.5 μM choline (20 nM [methyl-^{3}H]choline) (f) by control HEK293T cells, *FLVCR1*-knockout HEK293T cells expressing a vector control, and *FLVCR1*-knockout HEK293T cells expressing *FLVCR1*

cDNA, normalized to the uptake of control HEK293T cells. n=3 biologically independent samples. Mean values are annotated. **d,g,** Uptake of 2 μM ethanolamine (1.86 nM ethanolamine [1-^{3}H] hydrochloride) (d) or 21.5 μM choline (20 nM [methyl-^{3}H]choline) (g) by *FLVCR1*-knockout HEK293T cells expressing a vector control (grey) or *FLVCR1* cDNA (black), incubated for the indicated time points. n=3 biologically independent samples. **e,h,** Background subtracted uptake of ethanolamine (e) or choline (h) by *FLVCR1*-knockout HEK293T cells expressing *FLVCR1* cDNA incubated with the indicated total ethanolamine (g) or choline (h) concentrations (0.093% radioactive substrate) for 1 minute. Background was measured by uptake of ethanolamine (e) or choline (h) by *FLVCR1*-knockout HEK293T cells expressing a vector control. n=3 biologically independent samples. Michaelis-Menten model fitted to the data is shown in red. **i,** Substrate-binding site in the ethanolamine-bound state. Residues and modelled substrates are shown as sticks. Density is shown as a grey isosurface and contoured at 3.0 **σ**. **j-k,** Superposition of substrate-binding sites in the choline-bound (blue) and ethanolamine-bound (gold) states, shown in two views. Substrate-binding site residues and modelled substrates are shown as sticks.

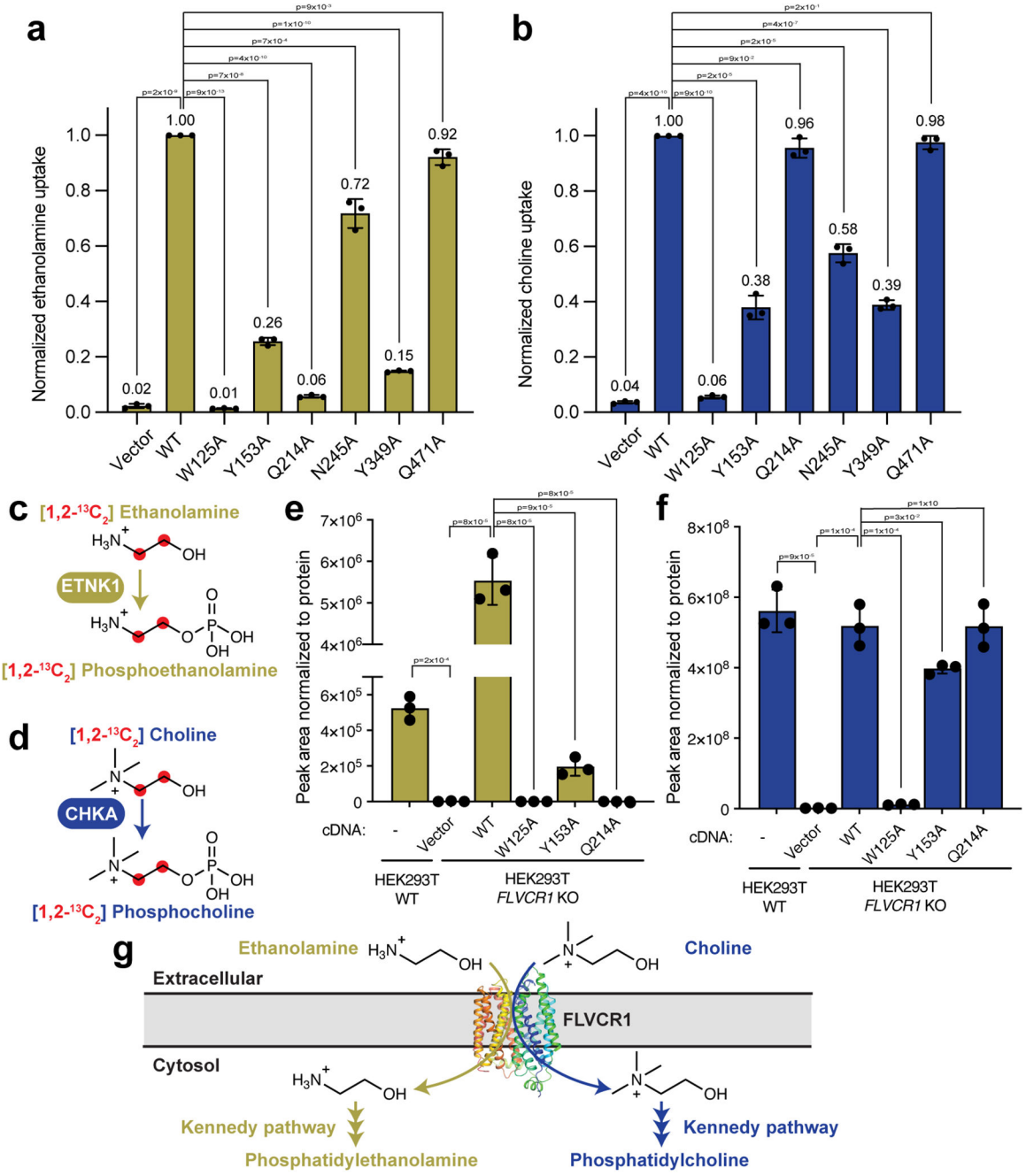

Fig. 4: FLVCR1 fuels both branches of the Kennedy pathway.

a-b, Uptake of 2 μM ethanolamine (1.86 nM ethanolamine [1-^{3}H] hydrochloride) (a) or 2 μM choline (1.86 nM ([methyl-^{3}H]choline) (b) by *FLVCR1*-knockout HEK293T cells expressing a vector control or wild-type or mutant *FLVCR1* cDNA for 30 minutes normalized to the uptake by *FLVCR1*-knockout HEK293T cells expressing wild-type *FLVCR1*. n=3 biologically independent samples. Mean values are annotated. **c-d,** Schematic for tracing [1,2-$^{13}C_2$] ethanolamine (c) or [1,2-$^{13}C_2$] choline (d) into downstream metabolites. **e,** Abundance of phosphoethanolamine M+2 after incubation with 2 μM

[1,2-$^{13}C_2$] ethanolamine for 1 hour in *FLVCR1*-knockout HEK293T cells expressing a vector control or wild-type or mutant *FLVCR1* cDNA. n=3 biologically independent samples. **f,** Abundance of phosphocholine M+2 after incubation with 21.5 μM [1,2-$^{13}C_2$] choline for 1 hour in *FLVCR1*-knockout HEK293T cells expressing a vector control or wild-type or mutant *FLVCR1* cDNA. n=3 biologically independent samples. **g,** Schematic of the phosphatidylcholine and phosphatidylethanolamine biosynthetic pathways.